POLITECNICO DI TORINO
Repository ISTITUZIONALE

A Virtual Element Method coupled with a Boundary Integral Non Reflecting condition for 2D exterior Helmholtz problems

Original
A Virtual Element Method coupled with a Boundary Integral Non Reflecting condition for 2D exterior Helmholtz problems / Desiderio, L., Falletta, S., Scuderi, L.. - In: COMPUTERS & MATHEMATICS WITH APPLICATIONS. - ISSN 0898-1221. - 84:(2021), pp. 296-313. [10.1016/j.camwa.2021.01.002]

Availability:
This version is available at: 11583/2949026 since: 2025-02-13T11:48:47Z

Publisher:
Elsevier

Published
DOI:10.1016/j.camwa.2021.01.002

Terms of use:

This article is made available under terms and conditions as specified in the corresponding bibliographic description in the repository

Publisher copyright
Elsevier postprint/Author's Accepted Manuscript

© 2021. This manuscript version is made available under the CC-BY-NC-ND 4.0 license
http://creativecommons.org/licenses/by-nc-nd/4.0/.The final authenticated version is available online at:
http://dx.doi.org/10.1016/j.camwa.2021.01.002

(Article begins on next page)

26 November 2026

A Virtual Element Method coupled with a Boundary Integral Non Reflecting condition for 2D exterior Helmholtz problems

L. Desiderio[a,*], S. Falletta[b], L. Scuderi[b]

[a] *Dipartimento di Scienze Matematiche, Fisiche e Informatiche, Università di Parma, Parco Area delle Scienze, 53/A, Parma, Italia*
[b] *Dipartimento di Scienze Matematiche "G.L. Lagrange", Politecnico di Torino, Corso Duca degli Abruzzi, 24, 10129, Torino, Italia*

Abstract

We present a new numerical approach to solve 2D exterior Helmholtz problems defined in unbounded domains. This consists in reducing the infinite region to a finite computational one Ω, by the introduction of an artificial boundary $\mathcal{B}$, and by applying in Ω a Virtual Element Method (VEM). The latter is coupled with a Boundary Integral Non Reflecting Condition defined on $\mathcal{B}$ (in short BI-NRBC), discretized by a standard collocation Boundary Element Method (BEM). We show that, by choosing the same approximation order of the VEM and of the BI-NRBC discretization spaces, the corresponding method allows to obtain the optimal order of convergence. We test the efficiency and accuracy of the proposed approach on various numerical examples, arising both from literature and real life application problems.

Keywords: Exterior Helmholtz problems, Virtual Element Method, Boundary Element Method, Non Reflecting Boundary Condition.

1. Introduction

In the last years the introduction of the Virtual Element Method (VEM) [7, 9] has allowed to broaden the classical family of the Finite Element Method (FEM) for the discretization of problems described by Partial Differential Equations (PDEs). In particular, VEMs generalize FEMs for what concerns both the decomposition of the computational domain and the definition of the local discrete spaces. Indeed, FEMs are typically constructed on triangular/tetrahedral or quadrilateral/hexahedral meshes, while VEMs can be defined on more general meshes such as polygons/polyhedra. It has been shown that the main advantage of using such meshes is the possibility of significantly simplifying the decomposition of domains with complex geometry and the reduction of the complexity of the adaptive mesh refinements. Additionally, VEMs overcome the key difficulty faced in designing a polygonal version of the FEMs for what concerns the construction of the discrete spaces. In the standard FEMs, the approximant basis functions are polynomials defined by closed and relatively simple formulas on each triangular/tetrahedral or quadrilateral/hexahedral element. However, when the mesh contains elements of more general shape, these local polynomial spaces are awkward and not rich enough to produce numerical schemes characterized by optimal local approximation properties and by a low computational cost. On the contrary, in the VEM formulation, the global discrete function space is built starting from local spaces that are "virtual", in the sense that they contain polynomials as in the FEM, but include also more general functions, whose pointwise values never need to be determined or evaluated in practice.

*Corresponding author.
Email addresses: luca.desiderio@unipr.it (L. Desiderio), silvia.falletta@polito.it (S. Falletta), letizia.scuderi@polito.it (L. Scuderi)

The VEM, introduced in [7] for the Poisson equation, has been applied to a wide variety of problems. We mention the pioneering papers concerning linear elasticity [8], inelasticity [5], plate bending problems [15], elliptic convection-reaction-diffusion problems [10], as well as Stokes problems [4] and fluid flows in fractured media [12, 13]. As far as the authors are aware, in the literature all papers dealing with VEMs treat problems set in bounded domains and, in particular, there is no application of these methods to simulate wave propagation phenomena in infinite or unbounded regions, which are often encountered in mathematical models associated with acoustic, aerodynamic, geophysical, electromagnetic and many other engineering and science disciplines. One class of numerical methods to solve exterior homogeneous problems is based on a re-formulation of the original PDE as an equivalent Boundary Integral Equation (BIE), whose unknown represents a contour/ surface distribution on the boundary. It is however known that, once the boundary distribution is retrieved by means of a Boundary Element Method (BEM) [29, 31], the solution of the original problem at any point of the exterior domain is obtained by computing boundary integrals. This procedure may result not efficient, especially when the solution is needed at many points of the infinite domain. Alternatively, when one is interested in studying the wave phenomenon in a particular subregion and/or when the medium presents inhomogeneities within a bounded region, it is possible to reduce the unbounded domain into a bounded computational one, delimited by a chosen artificial boundary. On this latter a suitable Non Reflecting Boundary Condition (NRBC) is imposed and the new problem, defined in the bounded region, is solved by a domain method such as Finite Differences (FD) or Finite Elements (FE).

The NRBC must guarantee that the solution of the problem, defined in the finite computational domain, coincides with the restriction to the computational domain of the solution of the original PDE. The NRBCs are usually divided into two main categories: the local (approximated) and the global (exact) ones. For the formers we refer to [24, 25]. The latter are generally defined by a known Boundary Integral (BI) relationship that the solution and its normal derivative must satisfy at the artificial boundary. The BI-NRBCs are nowadays widely used since they offer many advantages with respect to the local ones. Among them, we mention that they allow to consider artificial boundaries of arbitrary shape and they are transparent, in the sense that they prevent spurious reflections caused by the reduction of the physical domain to a bounded one, both when convex or non-convex artificial boundaries are considered. Moreover, they can be used in situations of multiple scattering and of non trivial data, whose (local) supports do not have necessarily to be included in the finite computational domain. They have been applied to several stationary and time dependent problems in combination with FD or FE methods (see, for example, [2, 6, 21]).

By virtue of the above mentioned benefits with respect to standard FEMs, in this paper we propose the use of a VEM coupled with a BI-NRBC to solve exterior 2D Dirichlet problems for the Helmholtz equation. We mention that, in literature, VEMs have been applied to the Helmholtz equation only in the case of interior problems and with a particular choice of the VEM discretization space that include plane-wave functions [27]. Here, we combine a standard VEM of order k with a BI-NRBC discretized by a classical collocation BEM of the same order k, within the context of conforming meshes. We remark that, in this case, the choice of VEM instead of FEM only affects the interior discretization and not the coupling, VEM and FEM traces being identical on the artificial boundary. Moreover, the numerical scheme that we propose allows in principle virtual element spaces of order k coupled with boundary element space of order 1. At the current stage of the implementation of the method, the choice of the same order for both the VEM and the BI-NRBC becomes mandatory to preserve the global accuracy.

The paper is organized as follows: in Section 2 we present the model problem for the Helmholtz equation, its restriction to a bounded region of interest by the introduction of the BI-NRBC and the variational formulation associated to the problem reformulated in the finite computational domain. In Section 3 we describe the main features of the VEM and of the BI-NRBC and their corresponding discretizations. In Section 4 we present various numerical simulations to validate the proposed approach. In the first example we show the optimal order of convergence of the scheme in the L^2-norm for a benchmark problem associated to different wave numbers. Moreover we highlight that, when high-frequencies are considered, we achieve a prescribed accuracy of the numerical solution by increasing the order of the VEM/BI-NRBC discretization spaces, rather than the mesh

density, with a not significant increasing of the complexity. Finally, some interesting applications to exterior acoustics are provided. The considered challenging problems are: i) spinning wave propagation; ii) scattering of plane waves by single or multiple rigid obstacles. The extensive testing have confirmed the robustness of the proposed approach as well as its feasibility to be applied to a wider set of exterior problems, reduced to finite computational domain of generic (even non-convex) shapes.

2. The model problem

In a fixed Cartesian coordinates system $\mathbf{x} = (x_1, x_2)^\top$, we consider an open bounded domain $\Omega_i \subset \mathbf{R}^2$ with boundary $\Gamma := \partial\Omega_i$ and we denote by $\Omega_e := \mathbf{R}^2 \setminus \overline{\Omega_i}$ the exterior unbounded domain. We are interested in the numerical solution of the following frequency-domain wave propagation problem in Ω_e:

$$\begin{cases} \Delta u_e(\mathbf{x}) + \kappa^2 u_e(\mathbf{x}) = 0 & \mathbf{x} \in \Omega_e \quad (1a) \\ u_e(\mathbf{x}) = g(\mathbf{x}) & \mathbf{x} \in \Gamma \quad (1b) \\ \lim\limits_{\|\mathbf{x}\|\to\infty} \|\mathbf{x}\|^{\frac{1}{2}} \left(\nabla u_e \cdot \dfrac{\mathbf{x}}{\|\mathbf{x}\|} - \imath\kappa u_e \right) = 0. & \quad (1c) \end{cases}$$

In the above problem, Equation (1a) is known as Helmholtz equation, Equation (1b) represents a boundary condition of Dirichlet type with datum g, and Equation (1c) is the Sommerfield radiation condition, that ensures the appropriate behaviour of the complex-valued unknown function u_e at infinity. Furthermore, ∇ and Δ denote the nabla and Laplace operators, respectively, and $\imath$ stands for the imaginary unit.
We recall that the given wave number κ is related to the speed of the wave propagation c by the relation $\kappa = \omega/c$, being ω the angular frequency. The corresponding wavelength $\lambda = 2\pi/\kappa$ allows to distinguish two regimes of interest: when λ is small compared to the size of Ω_i, i.e. $\kappa\,\mathrm{diam}(\Omega_i) > 2\pi$, we are in the so-called high-frequency regime; when $\kappa\,\mathrm{diam}(\Omega_i) < 2\pi$, we deal with problems in the low-frequency regime.
In the sequel we assume that $g \in H^{1/2}(\Gamma)$ to guarantee existence and uniqueness of the solution $u_e \in H^1_{\mathrm{loc}}(\Omega_e)$ of Problem (1) (see [17]).

As many practical situations require, we aim at determining the solution u_e of Problem (1) in a bounded subregion of Ω_e surrounding Ω_i. To this end, we introduce an artificial boundary $\mathcal{B}$ which allows to decompose Ω_e into a finite computational domain Ω, bounded internally by Γ and externally by $\mathcal{B}$, and an infinite residual one, denoted by Ω_∞, as depicted in Figure 1.

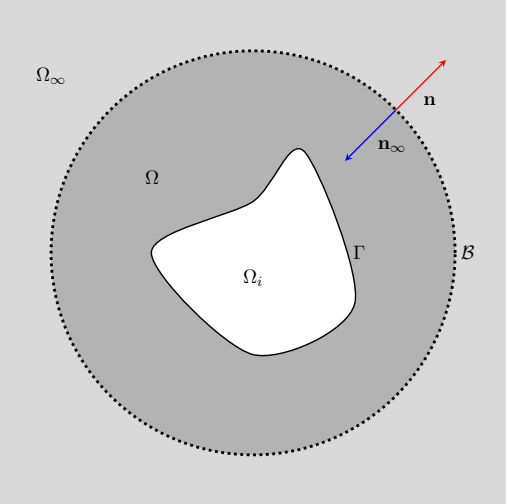

Figure 1: Model problem setting.

Introducing u and u_∞, which represent the restrictions of the solution u_e to Ω and Ω_∞, respectively, and denoting by $\mathbf{n}$ and $\mathbf{n}_\infty$ the unit normal vectors to $\mathcal{B}$ pointing outside Ω and Ω_∞, we impose the following compatibility and equilibrium conditions (recall that $\mathbf{n}_\infty = -\mathbf{n}$):

$$u(\mathbf{x}) = u_\infty(\mathbf{x}) \qquad \mathbf{x} \in \mathcal{B} \tag{2a}$$

$$\frac{\partial u}{\partial \mathbf{n}}(\mathbf{x}) = -\frac{\partial u_\infty}{\partial \mathbf{n}_\infty}(\mathbf{x}) \qquad \mathbf{x} \in \mathcal{B}. \tag{2b}$$

To obtain a well posed problem in Ω, we need to impose a proper boundary condition on $\mathcal{B}$. It is known that the solution u_∞ in Ω_∞ can be represented by the following Kirchhoff's formula:

$$u_\infty(\mathbf{x}) = \int_{\mathcal{B}} G(\mathbf{x},\mathbf{y}) \frac{\partial u_\infty}{\partial \mathbf{n}_{\infty,\mathbf{y}}}(\mathbf{y})\, \mathrm{d}\mathcal{B}_\mathbf{y} - \int_{\mathcal{B}} \frac{\partial G}{\partial \mathbf{n}_{\infty,\mathbf{y}}}(\mathbf{x},\mathbf{y}) u_\infty(\mathbf{y})\, \mathrm{d}\mathcal{B}_\mathbf{y} \qquad \mathbf{x} \in \Omega_\infty \setminus \mathcal{B}, \tag{3}$$

in which G is the fundamental solution of the 2D Helmholtz problem. The expression of G and of its normal derivative in (3) are given by

$$G(\mathbf{x},\mathbf{y}) = \frac{\imath}{4} H_0^{(1)}(\kappa r) \quad \text{and} \quad \frac{\partial G}{\partial \mathbf{n}_{\infty,\mathbf{y}}}(\mathbf{x},\mathbf{y}) = \frac{\imath\kappa}{4} \frac{\mathbf{r}\cdot\mathbf{n}_{\infty,\mathbf{y}}}{r} H_1^{(1)}(\kappa r), \tag{4}$$

where $r = \|\mathbf{x}-\mathbf{y}\|$ represents the distance between the source point $\mathbf{x}$ and the field point $\mathbf{y}$, and $H_m^{(1)}$ denotes the m-th order Hankel function of the first kind. Introducing the single-layer integral operator $V\colon H^{-1/2}(\mathcal{B}) \to H^{1/2}(\mathcal{B})$

$$V\psi(\mathbf{x}) := \int_{\mathcal{B}} G(\mathbf{x},\mathbf{y})\psi(\mathbf{y})\, \mathrm{d}\mathcal{B}_\mathbf{y}, \qquad \mathbf{x} \in \mathcal{B} \tag{5}$$

and the double-layer integral operator $K\colon H^{1/2}(\mathcal{B}) \to H^{1/2}(\mathcal{B})$

$$K\varphi(\mathbf{x}) := \int_{\mathcal{B}} \frac{\partial G}{\partial \mathbf{n}_{\infty,\mathbf{y}}}(\mathbf{x},\mathbf{y})\varphi(\mathbf{y})\, \mathrm{d}\mathcal{B}_\mathbf{y}, \qquad \mathbf{x} \in \mathcal{B}, \tag{6}$$

the trace of (3) on $\mathcal{B}$ reads (see [17])

$$\frac{1}{2}u_\infty(\mathbf{x}) - V\frac{\partial u_\infty}{\partial \mathbf{n}_{\infty,\mathbf{y}}}(\mathbf{x}) + Ku_\infty(\mathbf{x}) = 0, \qquad \mathbf{x} \in \mathcal{B}. \tag{7}$$

Equation (7), which expresses the natural relation that u_∞ and its normal derivative have to satisfy at each point of the artificial boundary, is imposed on $\mathcal{B}$ as an exact (non local) BI-NRBC to solve Problem (1) in the finite computational domain.

Thus, taking into account the compatibility and equilibrium conditions (2a)-(2b), and introducing the notation $w(\mathbf{x}) := \frac{\partial u}{\partial \mathbf{n}}(\mathbf{x})$, the new problem defined in the domain of interest Ω takes the form:

$$\begin{cases} \Delta u(\mathbf{x}) + \kappa^2 u(\mathbf{x}) = 0 & \mathbf{x} \in \Omega \quad (8a) \\ u(\mathbf{x}) = g(\mathbf{x}) & \mathbf{x} \in \Gamma \quad (8b) \\ \frac{1}{2} u(\mathbf{x}) + V w(\mathbf{x}) + K u(\mathbf{x}) = 0 & \mathbf{x} \in \mathcal{B}. \quad (8c) \end{cases}$$

We point out that w, which is defined on the boundary $\mathcal{B}$ in general by means of a trace operator (see [28]), is an additional unknown function. In order to use a variational method for (8a)-(8b) and to apply a collocation approach for (8c), we consider the weak form only for the Helmholtz equation and we impose the BI-NRBC in its strong form, i.e. pointwise. To this end, we set

$$H^1_{0,\Gamma}(\Omega) := \left\{ u \in H^1(\Omega) \ : \ u_{|\Gamma} = 0 \right\} \qquad \text{and} \qquad H^1_{g,\Gamma}(\Omega) := \left\{ u \in H^1(\Omega) \ : \ u_{|\Gamma} = g \right\}, \tag{9}$$

we introduce the bilinear forms $a, m : H^1(\Omega) \times H^1(\Omega) \to \mathbf{C}$ given by

$$a(u,v) := \int_\Omega \nabla u(\mathbf{x}) \cdot \nabla v(\mathbf{x}) \, \mathrm{d}\mathbf{x} \qquad \text{and} \qquad m(u,v) := \int_\Omega u(\mathbf{x}) v(\mathbf{x}) \, \mathrm{d}\mathbf{x}, \tag{10}$$

and the $L^2(\mathcal{B})$-inner product $(\cdot,\cdot)_\mathcal{B} : L^2(\mathcal{B}) \times L^2(\mathcal{B}) \to \mathbf{C}$

$$(w,v)_\mathcal{B} = \int_\mathcal{B} w(\mathbf{x}) v(\mathbf{x}) \mathrm{d}\mathcal{B}_\mathbf{x}, \tag{11}$$

extended to the duality pairing on $H^{-1/2}(\mathcal{B}) \times H^{1/2}(\mathcal{B})$ denoted by $\langle \cdot, \cdot \rangle_\mathcal{B}$.

The variational formulation of Problem (8) consists in finding $u \in H^1_{g,\Gamma}(\Omega)$ and $w \in H^{-1/2}(\mathcal{B})$ such that

$$\begin{cases} -a(u,v) + \kappa^2 m(u,v) + \langle w, v \rangle_\mathcal{B} = 0 & \forall\, v \in H^1_{0,\Gamma}(\Omega) \quad (12a) \\ \frac{1}{2} u(\mathbf{x}) + V w(\mathbf{x}) + K u(\mathbf{x}) = 0 & \mathbf{x} \in \mathcal{B}. \quad (12b) \end{cases}$$

3. Discretization

3.1. Discrete variational formulation

We start by assuming that the bounded domain Ω_i is a polygon and that the artificial boundary $\mathcal{B}$ is of piecewise linear type, so that Ω is a domain with polygonal boundaries. We remark that this choice avoids the issue of the approximation of the geometry and allows to retrieve the optimal rate of convergence of the method by using standard (non curvilinear) elements both in the interior VEM and for the approximation of the BI-NRBC.

It is worth mentioning that, while for the resolution of an exterior problem by a BEM, smoothness assumptions on the domain boundary are required to obtain the regularity of the BI operators and, consequently, to guarantee the expected convergence order of the method, we have observed that the latter are not necessary here in the VEM coupled with BI-NRBC. To this regard, we mention that in [30] the author himself asserts that "*nobody has reported experimental failure of the Johnson-Nédélec's coupling when the hypotheses* (on the artificial boundary $\mathcal{B}$) *are not met*". Moreover, he proves that for a simple model problem, the above mentioned coupling works for any Lipschitz $\mathcal{B}$, when applying the direct boundary integral equation with single and double layer integral operators (see also [32] for further interesting results).

It is reasonable to believe that the theoretical results obtained in [30] hold for our problem as well.

In order to obtain the discrete counterpart of Problem (12), we consider an unstructured mesh $\mathcal{T}_h = \{E\}$, that represents a coverage of the domain Ω with a finite number N_{E} of simply connected polygons. The mesh width h is related to the spacing of the grid.
We suppose that each element $E \in \mathcal{T}_h$ has n_{E} vertices $\mathbf{V}_1, \dots, \mathbf{V}_{n_{\mathrm{E}}}$ and its boundary ∂E is made of n_{E} line segments $e_1, \dots, e_{n_{\mathrm{E}}}$. Furthermore, we denote by $\mathbf{V}_E$, h_E and $|E|$ the mass center, the diameter and the measure of E, respectively. Additionally, we call N_{V} and N_{e} the numbers of total vertices and edges of $\mathcal{T}_h$, respectively.
Finally, we denote by $\mathcal{T}_h^{\mathcal{B}}$ the decomposition of the artificial boundary $\mathcal{B}$, inherited from $\mathcal{T}_h$, which consists of $N_{\mathcal{B}}$ straight segments.

Let $V_h^k \subset H^1(\Omega)$ and $W_h^k \subset H^{-1/2}(\mathcal{B})$ denote two (finite dimensional) discrete spaces associated to the meshes $\mathcal{T}_h$ and $\mathcal{T}_h^{\mathcal{B}}$. The parameter $k \geq 1$ denotes the degree of the polynomials defined on each element E that are contained in the spaces V_h^k, and it is related to the order of accuracy of the method. We consider the following discrete problem: find $u_h \in V_{h,g}^k$ and $w_h \in W_h^k$ such that

$$\begin{cases} -a_h(u_h, v_h) + \kappa^2 m_h(u_h, v_h) + \langle w_h, v_h \rangle_h = 0 & \forall\, v_h \in V_{h,0}^k \qquad (13a) \\ \dfrac{1}{2} u_h(\mathbf{x}) + V w_h(\mathbf{x}) + K u_h(\mathbf{x}) = 0 & \mathbf{x} \in \mathcal{B}, \qquad (13b) \end{cases}$$

having set

$$V_{h,0}^k := V_h^k \cap H_{0,\Gamma}^1(\Omega) \qquad \text{and} \qquad V_{h,g}^k := V_h^k \cap H_{g,\Gamma}^1(\Omega). \tag{14}$$

In Equation (13a), $a_h, m_h : V_h^k \times V_h^k \to \mathbf{C}$ are two discrete bilinear forms approximating a and m respectively, while $\langle \cdot, \cdot \rangle_h : W_h^k \times V_h^k \to \mathbf{C}$ represents an approximation of $\langle \cdot, \cdot \rangle_{\mathcal{B}}$.

In the next sections we describe in detail the virtual element space V_h^k and the boundary element space W_h^k.

3.2. Discretization by the Virtual Element Method in the computational domain

Before formally characterizing the discrete space V_h^k, we observe that the introduction of the mesh $\mathcal{T}_h$ allows to split the bilinear forms a and m defined in (10) into a sum of local bilinear forms $a^{\mathrm{E}}, m^{\mathrm{E}} : H^1(E) \times H^1(E) \to \mathbf{C}$, such that

$$a(u, v) = \sum_{E \in \mathcal{T}_h} a^{\mathrm{E}}(u, v) = \sum_{E \in \mathcal{T}_h} \int_E \nabla u(\mathbf{x}) \cdot \nabla v(\mathbf{x}) \, \mathrm{d}\mathbf{x} \tag{15}$$

$$m(u, v) = \sum_{E \in \mathcal{T}_h} m^{\mathrm{E}}(u, v) = \sum_{E \in \mathcal{T}_h} \int_E u(\mathbf{x}) v(\mathbf{x}) \, \mathrm{d}\mathbf{x}. \tag{16}$$

Denoting by $\mathcal{P}_k(E)$ the space of polynomials of degree k defined on E (for $k = -1$ we set $\mathcal{P}_{-1}(E) := \{0\}$), we introduce the H^1-projection operator $\Pi_k^{\nabla, E} : H^1(E) \to \mathcal{P}_k(E)$, such that

$$a^{\mathrm{E}}\left(\Pi_k^{\nabla, E} v, q\right) = a^{\mathrm{E}}(v, q) \qquad \forall\, q \in \mathcal{P}_k(E). \tag{17}$$

Being $\Pi_k^{\nabla, E}$ defined up to a constant, to determine it uniquely, it is necessary to introduce a projector onto constants $P_0^E := \Pi_0^{\nabla, E} : H^1(E) \to \mathcal{P}_0(E)$ such that $P_0^E(\Pi_k^{\nabla, E} v) = P_0^E(v)$. Following

[9], we define P_0^E as

$$\begin{cases} P_0^E(v) := \dfrac{1}{N_{\mathrm{E}}} \displaystyle\sum_{j=1}^{N_{\mathrm{E}}} v(\mathbf{V}_j) & \text{for } k = 1 \\ P_0^E(v) := \dfrac{1}{|E|} \displaystyle\int_E v(\mathbf{x})\, \mathrm{d}\mathbf{x} & \text{for } k \geq 2. \end{cases} \tag{18}$$

Additionally, we introduce the L^2-projection operator $\Pi_k^{0,E} : L^2(E) \to \mathcal{P}_k(E)$, defined such that

$$m^{\mathrm{E}}\left(\Pi_k^{0,E} v, q\right) = m^{\mathrm{E}}(v, q) \qquad \forall\, q \in \mathcal{P}_k(E). \tag{19}$$

The space V_h^k is built element-wise, by preliminarily introducing for each $E \in \mathcal{T}_h$ the local finite dimensional *augmented* virtual space $\widetilde{V}_h^k(E)$ and the local *enhanced* virtual space $V_h^k(E)$ defined as (see [1], Section 3 for details)

$$\widetilde{V}_h^k(E) := \left\{ v_h \in H^1(E) \ : \ v_h{}_{|\partial E} \in C^0(\partial E),\ v_h{}_{|e} \in \mathcal{P}_k(e)\ \forall\, e \subset \partial E,\ \Delta v_h \in \mathcal{P}_k(E) \right\} \tag{20}$$

and

$$V_h^k(E) := \left\{ v_h \in \widetilde{V}_h^k(E) \ : \ m^{\mathrm{E}}\left(\Pi_k^{\nabla,E} v_h, q\right) = m^{\mathrm{E}}(v_h, q)\ \ \forall\, q \in \mathcal{P}_k(E)/\mathcal{P}_{k-2}(E) \right\}, \tag{21}$$

where $\mathcal{P}_k(E)/\mathcal{P}_{k-2}(E)$ stands for the space of all polynomials of degree k on E that are L^2-orthogonal to all polynomials of degree $k-2$ on E. It is possible to prove that the dimension of $V_h^k(E)$ is (see [1], Proposition 2)

$$n := \dim(V_h^k(E)) = k n_{\mathrm{E}} + \frac{k(k-1)}{2} \tag{22}$$

and that a generic element v_h of $V_h^k(E)$ is uniquely determined by the following n conditions (see [1]):

- its values at the n_{E} vertices of E;
- its values at $k-1$ uniformly spaced internal points of every edge $e \subset \partial E$, for $k > 1$;
- its moments up to order $k-2$ in E, defined for $k \geq 2$ as:

$$\frac{1}{|E|} \int_E v_h(\mathbf{x}) q(\mathbf{x})\, \mathrm{d}\mathbf{x} \qquad \forall\, q \in \mathcal{P}_{k-2}(E). \tag{23}$$

As shown in [1], the space $\mathcal{P}_k(E)$ is included in $V_h^k(E)$. Now, choosing an arbitrary but fixed ordering of the degrees of freedom such that these are indexed by $i = 1, \cdots, n$, we introduce as in [7] the operator $\mathrm{dof}_i : V_h^k(E) \longrightarrow \mathbf{R}$, $i = 1, \cdots, n$, defined as

$$\mathrm{dof}_i(v_h) := \text{the value of the } i\text{-th local degree of freedom of } v_h.$$

The basis functions $\{\Phi_j\}_{j=1}^n$ chosen for the space $V_h^k(E)$ are the standard Lagrangian ones, such that

$$\mathrm{dof}_i(\Phi_j) = \delta_{ij}, \qquad i, j = 1, \ldots, n, \tag{24}$$

δ_{ij} being the Kronecker delta. The key feature of the VEM consists in computing the local bilinear forms a^{E} and m^{E} without the need of knowing a closed form of the basis functions. Indeed, we remark that, according to the definition of $V_h^k(E)$, it is not possible to compute the quantities $a^{\mathrm{E}}(u_h, v_h)$ and $m^{\mathrm{E}}(u_h, v_h)$, being an element of $V_h^k(E)$ not explicitly known in the interior of E. On

the contrary, the bilinear forms $a^{\mathrm{E}}(q, v_h)$ and $m^{\mathrm{E}}(q, v_h)$ are exactly computable when $q \in \mathcal{P}_k(E)$ and $v_h \in V_h^k(E)$, since in this case the expression of v_h inside E is not needed. Indeed, by using the Green's formula

$$a^{\mathrm{E}}(q, v_h) = \int_E \nabla q(\mathbf{x}) \cdot \nabla v_h(\mathbf{x}) \, \mathrm{d}\mathbf{x} = -\int_E \Delta q(\mathbf{x}) v_h(\mathbf{x}) \, \mathrm{d}\mathbf{x} + \int_{\partial \mathrm{E}} \frac{\partial q}{\partial \mathbf{n}}(\mathbf{x}) v_h(\mathbf{x}) \, \mathrm{d}\mathbf{x},$$

we get that the right hand side integrals are computable: the first according to (23) since $\Delta q \in \mathcal{P}_{k-2}(E)$; the second one since $\partial q / \partial \mathbf{n} \in \mathcal{P}_{k-1}(E)$ and $v_h \in \mathcal{P}_k(\partial E)$.
Again, the condition in (23) allows to compute

$$m^{\mathrm{E}}(q, v_h) = \int_E q(\mathbf{x}) v_h(\mathbf{x}) \, \mathrm{d}\mathbf{x} \qquad \forall q \in \mathcal{P}_{k-2}(E).$$

Since $V_h^k(E) \subset \widetilde{V}_h^k(E) \subset H^1(E)$, the H^1-projection $\Pi_k^{\nabla,E}$ is well defined on $V_h^k(E)$ and we can evaluate

$$m^{\mathrm{E}}(q, v_h) = \int_E q(\mathbf{x}) v_h(\mathbf{x}) \, \mathrm{d}\mathbf{x} = \int_E q(\mathbf{x}) \Pi_k^{\nabla,E} v_h(\mathbf{x}) \, \mathrm{d}\mathbf{x} \qquad \forall \, q \in \mathcal{P}_k(E)/\mathcal{P}_{k-2}(E), \, \forall \, v_h \in V_h^k(E).$$

According to the above considerations, in order to define computable discrete local bilinear forms $a_h^{\mathrm{E}} : V_h^k(E) \times V_h^k(E) \to \mathbf{C}$ and $m_h^{\mathrm{E}} : V_h^k(E) \times V_h^k(E) \to \mathbf{C}$, following [7] and by using the definition of $\Pi_k^{\nabla,E}$ and $\Pi_k^{0,E}$, we first split a^{E} and m^{E} in a part that can be computed exactly (up to the machine precision) and in a part that will be suitably approximated:

$$a^{\mathrm{E}}(u_h, v_h) := a^{\mathrm{E}}\left(\Pi_k^{\nabla,E} u_h, \Pi_k^{\nabla,E} v_h\right) + a^{\mathrm{E}}\left(\left(I - \Pi_k^{\nabla,E}\right) u_h, \left(I - \Pi_k^{\nabla,E}\right) v_h\right) \tag{25}$$

$$m^{\mathrm{E}}(u_h, v_h) := m^{\mathrm{E}}\left(\Pi_k^{0,E} u_h, \Pi_k^{0,E} v_h\right) + m^{\mathrm{E}}\left(\left(I - \Pi_k^{0,E}\right) u_h, \left(I - \Pi_k^{0,E}\right) v_h\right), \tag{26}$$

I being the identity operator. The implementation steps for the computation of $a^{\mathrm{E}}\left(\Pi_k^{\nabla,E} u_h, \Pi_k^{\nabla,E} v_h\right)$ and $m^{\mathrm{E}}\left(\Pi_k^{0,E} u_h, \Pi_k^{0,E} v_h\right)$ require the choice of a suitable basis of the space $\mathcal{P}_k(E)$, that allows to define in practice the projectors $\Pi_k^{\nabla,E}$ and $\Pi_k^{0,E}$. In accordance with the standard literature on VEM (see [9], Section 3.1), we have considered the basis of the scaled monomials, i.e.

$$\mathcal{M}_k(E) := \left\{ m_{\boldsymbol{\alpha}}(\mathbf{x}) = \left(\frac{x_1 - V_{E,1}}{h_E}\right)^{\alpha_1} \left(\frac{x_2 - V_{E,2}}{h_E}\right)^{\alpha_2}, \; \boldsymbol{\alpha} = (\alpha_1, \alpha_2) \; : \; |\boldsymbol{\alpha}| = \alpha_1 + \alpha_2 \leq k \right\},$$

where, we recall, $\mathbf{V}_E = (V_{E,1}, V_{E,2})$ and h_E denote the mass centre and the diameter of E, respectively. This choice allows for an exact (up to the machine precision) and easy computation of the first terms in the right hand side of (25) and (26), provided we have an efficient rule to compute the L^2-product of two scaled monomials, i.e.

$$\mathcal{H}_{\boldsymbol{\alpha}\boldsymbol{\beta}} := \int_E m_{\boldsymbol{\alpha}}(\mathbf{x}) m_{\boldsymbol{\beta}}(\mathbf{x}) \mathrm{d}\mathbf{x} = \int_E \left(\frac{x_1 - V_{E,1}}{h_E}\right)^{\alpha_1+\beta_1} \left(\frac{x_2 - V_{E,2}}{h_E}\right)^{\alpha_2+\beta_2} \mathrm{d}x_1 \mathrm{d}x_2. \tag{27}$$

Recalling that ∂E consists of n_{E} segments $e_1, \ldots, e_{n_{\mathrm{E}}}$, by applying to (27) the divergence theorem, we obtain the following explicit formula we have considered to compute $\mathcal{H}_{\boldsymbol{\alpha}\boldsymbol{\beta}}$:

$$\mathcal{H}_{\boldsymbol{\alpha}\boldsymbol{\beta}} = \frac{1}{\alpha_1 + \beta_1 + 1} \left(\frac{1}{h_E}\right)^{|\boldsymbol{\alpha}|+|\boldsymbol{\beta}|} \sum_{i=1}^{n_{\mathrm{E}}} \int_{e_i} n_{i,1} \left(x_1 - V_{E,1}\right)^{\alpha_1+\beta_1+1} \left(x_2 - V_{E,2}\right)^{\alpha_2+\beta_2} \mathrm{d}e_i, \tag{28}$$

where $n_{i,1}$ is the component in the x_1-direction of the unit normal vector at e_i pointing outside E. Denoting by $\mathbf{V}_i$ and $\mathbf{V}_{i+1}$ the endpoints of e_i, we introduce the parametrization $\boldsymbol{\gamma} : [0,1] \to e_i$ such that

$$\boldsymbol{\gamma}(t) := \begin{cases} x_1(t) = V_{i,1} + (V_{i+1,1} - V_{i,1})t = V_{i,1} + \ell_{i,1}t \\ x_2(t) = V_{i,2} + (V_{i+1,2} - V_{i,2})t = V_{i,2} + \ell_{i,2}t \end{cases}$$

and we recast (28) in the following form:

$$\mathcal{H}_{\boldsymbol{\alpha}\boldsymbol{\beta}} = \frac{1}{\alpha_1 + \beta_1 + 1} \left(\frac{1}{h_E}\right)^{|\boldsymbol{\alpha}|+|\boldsymbol{\beta}|} \sum_{i=1}^{n_{\mathrm{E}}} \ell_{i,2} \int_0^1 \left(\overline{V}_{i,1} + \ell_{i,1}t\right)^{\alpha_1+\beta_1+1} \left(\overline{V}_{i,2} + \ell_{i,2}t\right)^{\alpha_2+\beta_2} \mathrm{d}t \tag{29}$$

where $\overline{\mathbf{V}}_i = \mathbf{V}_i - \mathbf{V}_E$. Finally, by using the binomial identity, we exactly compute the integrals in (29) as follows:

$$\mathcal{H}_{\boldsymbol{\alpha}\boldsymbol{\beta}} = \frac{1}{\eta_1 + 1} \left(\frac{1}{h_E}\right)^{|\boldsymbol{\eta}|} \sum_{i=1}^{n_{\mathrm{E}}} \sum_{r=0}^{\eta_1+1} \sum_{s=0}^{\eta_2} \binom{\eta_1+1}{r} \binom{\eta_2}{s} \frac{\overline{V}_{i,1}^{\eta_1+1-r} \overline{V}_{i,2}^{\eta_2-s}}{r+s+1} \ell_{i,1}^r \ell_{i,2}^{s+1} \tag{30}$$

where $\boldsymbol{\eta} = (\eta_1, \eta_2) := (\alpha_1 + \alpha_2, \beta_1 + \beta_2)$.

For what concerns the second terms in (25) and (26), these are approximated by the following bilinear forms

$$s^{\mathrm{E}}\left(\left(I - \Pi_k^{\nabla,E}\right) u_h, \left(I - \Pi_k^{\nabla,E}\right) v_h\right) := \sum_{j=1}^{n} \mathrm{dof}_j\left(\left(I - \Pi_k^{\nabla,E}\right) u_h\right) \mathrm{dof}_j\left(\left(I - \Pi_k^{\nabla,E}\right) v_h\right), \tag{31}$$

$$r^{\mathrm{E}}\left(\left(I - \Pi_k^{0,E}\right) u_h, \left(I - \Pi_k^{0,E}\right) v_h\right) := \sum_{j=1}^{n} \mathrm{dof}_j\left(\left(I - \Pi_k^{0,E}\right) u_h\right) \mathrm{dof}_j\left(\left(I - \Pi_k^{0,E}\right) v_h\right), \tag{32}$$

that allow to define the approximations a_h^{E} and m_h^{E} of a^{E} and m^{E}, respectively, as follows:

$$a_h^{\mathrm{E}}(u_h, v_h) := a^{\mathrm{E}}\left(\Pi_k^{\nabla,E} u_h, \Pi_k^{\nabla,E} v_h\right) + s^{\mathrm{E}}\left(\left(I - \Pi_k^{\nabla,E}\right) u_h, \left(I - \Pi_k^{\nabla,E}\right) v_h\right) \tag{33}$$

$$m_h^{\mathrm{E}}(u_h, v_h) := m^{\mathrm{E}}\left(\Pi_k^{0,E} u_h, \Pi_k^{0,E} v_h\right) + r^{\mathrm{E}}\left(\left(I - \Pi_k^{0,E}\right) u_h, \left(I - \Pi_k^{0,E}\right) v_h\right). \tag{34}$$

We recall that the quantities in (31) and (32) are called *stabilization terms* and are defined such that the following properties are satisfied (see [7]):

- k-consistency: for all $v_h \in V_h^k(E)$ and for all $q \in \mathcal{P}_k(E)$:

$$a_h^{\mathrm{E}}(v_h, q) = a^{\mathrm{E}}(v_h, q) \tag{35}$$

$$m_h^{\mathrm{E}}(v_h, q) = m^{\mathrm{E}}(v_h, q) \tag{36}$$

- stability: there exist four positive constants $\alpha_*, \beta_*, \alpha^*$ and β^* all independent of h, such that for all $v_h \in V_h^k(E)$:

$$\alpha_* a^{\mathrm{E}}(v_h, v_h) \le a_h^{\mathrm{E}}(v_h, v_h) \le \alpha^* a^{\mathrm{E}}(v_h, v_h) \tag{37}$$

$$\beta_* m^{\mathrm{E}}(v_h, v_h) \le m_h^{\mathrm{E}}(v_h, v_h) \le \beta^* m^{\mathrm{E}}(v_h, v_h). \tag{38}$$

On the basis of the definition of the local VEM space $V_h^k(E)$, the global VEM space is defined as

$$V_h^k := \left\{ v_h \in H^1(E) \ : \ v_h{}_{|E} \in V_h^k(E) \right\}. \tag{39}$$

Analogously, the global approximate bilinear forms $a_h : V_h^k \times V_h^k \to \mathbf{C}$ and $m_h : V_h^k \times V_h^k \to \mathbf{C}$ are defined by summing up the local contributions as follows:

$$a_h(u_h, v_h) := \sum_{E \in \mathcal{T}_h} a_h^{\mathrm{E}}(u_h, v_h) \qquad \text{and} \qquad m_h(u_h, v_h) := \sum_{E \in \mathcal{T}_h} m_h^{\mathrm{E}}(u_h, v_h). \tag{40}$$

We remark that the global degrees of freedom for a generic element $v_h \in V_h^k$ are:

- its values at each of the N_{V} vertices of $\mathcal{T}_h$;
- its values at $k-1$ distinct internal points of each of the N_{e} edges of $\mathcal{T}_h$, for $k > 1$;
- its moments up to order $k-2$ in each of the N_{E} elements of $\mathcal{T}_h$, for $k > 2$:

$$\frac{1}{|E|} \int_E v_h(\mathbf{x}) q(\mathbf{x}) \, \mathrm{d}\mathbf{x} \qquad \forall q \in \mathcal{P}_{k-2}(E). \tag{41}$$

Consequently, V_h^k has dimension

$$N := \dim(V_h^k) = N_{\mathrm{V}} + (k-1) N_{\mathrm{e}} + \frac{k(k-1)}{2} N_{\mathrm{E}}. \tag{42}$$

To derive the linear system associated to (13a)-(13b), we further need to introduce the boundary element space

$$W_h^k := \left\{ \psi \in \mathrm{L}^2(\mathcal{B}) \ : \ \psi_{|_e} \in \mathcal{P}_k(e), \ \forall e \in \mathcal{B} \right\} \qquad \text{with} \qquad |e| < h, \tag{43}$$

where $|e|$ denotes the length of the edge e.

For what follows, it is convenient to reorder and split the complete index set $\mathcal{S} := \{j = 1, \cdots, N\}$ of the basis functions $\{\Phi_j\}_{j \in \mathcal{S}}$ of V_h^k as

$$\mathcal{S} = \mathcal{S}^I \cup \mathcal{S}^\Gamma \cup \mathcal{S}^\mathcal{B}, \tag{44}$$

where $\mathcal{S}^I$, $\mathcal{S}^\Gamma$ and $\mathcal{S}^\mathcal{B}$ denote the sets of indices related to the internal degrees of freedom and to the degrees of freedom lying on Γ and $\mathcal{B}$, respectively. With this choice, it follows that

$$V_{h,0}^k = \operatorname{span}\{\Phi_j\}_{j \in \mathcal{S}^I \cup \mathcal{S}^\mathcal{B}}, \qquad W_h^k = \operatorname{span}\left\{\Phi_j^\mathcal{B}\right\}_{j \in \mathcal{S}^\mathcal{B}},$$

having denoted by $\Phi_j^\mathcal{B} := \Phi_j \,|_\mathcal{B}$.

In order to derive the system associated to the discrete problem (13), we expand the unknown functions as

$$u_h(\mathbf{x}) := \sum_{j \in \mathcal{S}} u_h^j \Phi_j(\mathbf{x}) \qquad \text{with} \quad u_h^j = \mathrm{dof}_j(u_h) \tag{45}$$

$$w_h(\mathbf{x}) := \sum_{j \in \mathcal{S}^\mathcal{B}} w_h^j \Phi_j^\mathcal{B}(\mathbf{x}) \qquad \text{with} \quad w_h^j = \mathrm{dof}_j(w_h) \tag{46}$$

and we impose the Dirichlet condition on Γ by introducing the approximation g_h of the datum g as

$$g_h(\mathbf{x}) := \sum_{j \in \mathcal{S}^\Gamma} g_h^j \Phi_j(\mathbf{x}) \qquad \text{with} \quad g_h^j = \mathrm{dof}_j(g).$$

Hence, we split

$$u_h(\mathbf{x}) := \sum_{j \in \mathcal{S}^\mathcal{B} \cup \mathcal{S}^I} u_h^j \Phi_j(\mathbf{x}) + \sum_{j \in \mathcal{S}^\Gamma} g_h^j \Phi_j(\mathbf{x})$$

and, using the basis functions of $V_{h,0}^k$ to test the discrete equation (13a), we get

$$\sum_{j\in\mathcal{S}^{\mathcal{B}}\cup\mathcal{S}^I} u_h^j \sum_{E\in\mathcal{T}_h}\left[-a_h^{\mathrm{E}}(\Phi_j,\Phi_i)+\kappa^2 m_h^{\mathrm{E}}(\Phi_j,\Phi_i)\right]+\sum_{j\in\mathcal{S}^{\mathcal{B}}} w_h^j\langle\Phi_j^{\mathcal{B}},\Phi_i\rangle_h$$
$$=\sum_{j\in\mathcal{S}^{\Gamma}} g_h^j \sum_{E\in\mathcal{T}_h}\left[a_h^{\mathrm{E}}(\Phi_j,\Phi_i)-\kappa^2 m_h^{\mathrm{E}}(\Phi_j,\Phi_i)\right], \qquad i\in\mathcal{S}^{\mathcal{B}}\cup\mathcal{S}^I. \tag{47}$$

To write the matrix form of the above linear system, we introduce the stiffness and mass matrices $\mathbb{A}$, $\mathbb{M}$ and the matrix $\mathbb{Q}$ whose entries are respectively defined by

$$\mathbb{A}_{ij}:=\sum_{E\in\mathcal{T}_h} a_h^{\mathrm{E}}(\Phi_j,\Phi_i), \qquad \mathbb{M}_{ij}:=\sum_{E\in\mathcal{T}_h} m_h^{\mathrm{E}}(\Phi_j,\Phi_i), \qquad \mathbb{Q}_{ij}:=\langle\Phi_j^{\mathcal{B}},\Phi_i\rangle_h$$

and the column vectors $\mathbf{u}=\left[u_h^j\right]_{j\in\mathcal{S}^{\mathcal{B}}\cup\mathcal{S}^I}$, $\mathbf{w}=\left[w_h^j\right]_{j\in\mathcal{S}^{\mathcal{B}}}$ and $\mathbf{g}=\left[g_h^j\right]_{j\in\mathcal{S}^{\Gamma}}$. In accordance with the splitting of the set of the degrees of freedom (44), we consider the block partitioned representation of the above matrices and vectors (with obvious meaning of the notation), and we rewrite equation (47) as follows:

$$\begin{bmatrix} -\mathbb{A}^{\mathcal{B}\mathcal{B}}+\kappa^2\mathbb{M}^{\mathcal{B}\mathcal{B}} & -\mathbb{A}^{\mathcal{B}I}+\kappa^2\mathbb{M}^{\mathcal{B}I} \\ -\mathbb{A}^{I\mathcal{B}}+\kappa^2\mathbb{M}^{I\mathcal{B}} & -\mathbb{A}^{II}+\kappa^2\mathbb{M}^{II} \end{bmatrix}\begin{bmatrix}\mathbf{u}^{\mathcal{B}}\\ \mathbf{u}^I\end{bmatrix}+\begin{bmatrix}\mathbb{Q}^{\mathcal{B}\mathcal{B}}\mathbf{w}\\ \mathbb{O}^{I\mathcal{B}}\mathbf{w}\end{bmatrix}=\begin{bmatrix}\left(\mathbb{A}^{\mathcal{B}\Gamma}-\kappa^2\mathbb{M}^{\mathcal{B}\Gamma}\right)\mathbf{g}\\ \left(\mathbb{A}^{I\Gamma}-\kappa^2\mathbb{M}^{I\Gamma}\right)\mathbf{g}\end{bmatrix} \tag{48}$$

being $\mathbb{O}^{I\mathcal{B}}$ the null matrix since $\langle\Phi_j^{\mathcal{B}},\Phi_i\rangle_h=0$ for $i\in\mathcal{S}^I$. For what concerns the generic entry $\mathbb{Q}_{ij}^{\mathcal{B}\mathcal{B}}$, we have

$$\mathbb{Q}_{ij}^{\mathcal{B}\mathcal{B}}=\langle\Phi_j^{\mathcal{B}},\Phi_i\rangle_h=\int_{\mathcal{B}}\Phi_j^{\mathcal{B}}(\mathbf{x})\Phi_i^{\mathcal{B}}(\mathbf{x})\,\mathrm{d}\mathcal{B}_{\mathbf{x}} \tag{49}$$

which is exactly computable, since $\Phi_j^{\mathcal{B}}\in\mathcal{P}_k(e)\ \forall e\subset\mathcal{B}$.

3.3. Discretization of the non reflecting boundary condition by a Boundary Element Method
Using the basis functions $\left\{\Phi_j^{\mathcal{B}}\right\}_{j\in\mathcal{S}^{\mathcal{B}}}$ to interpolate the unknown function $u_h(\mathbf{x})$ and its normal derivative $w_h(\mathbf{x})$ on the artificial boundary $\mathcal{B}$, i.e.

$$u_h\,|_{\mathcal{B}}(\mathbf{x}):=\sum_{j\in\mathcal{S}^{\mathcal{B}}} u_h^j\Phi_j^{\mathcal{B}}(\mathbf{x}) \qquad \text{with} \quad u_h^j=\mathrm{dof}_j(u_h) \tag{50}$$

$$w_h(\mathbf{x}):=\sum_{j\in\mathcal{S}^{\mathcal{B}}} w_h^j\Phi_j^{\mathcal{B}}(\mathbf{x}) \qquad \text{with} \quad w_h^j=\mathrm{dof}_j(w_h) \tag{51}$$

the discrete equation (13b) can be rewritten as

$$\sum_{j\in\mathcal{S}^{\mathcal{B}}}\left\{u_h^j\left[\frac{1}{2}\Phi_j^{\mathcal{B}}(\mathbf{x})+\int_{\mathcal{B}}\frac{\partial G}{\partial\mathbf{n}_{\mathbf{y}}}(\mathbf{x},\mathbf{y})\Phi_j^{\mathcal{B}}(\mathbf{y})\,\mathrm{d}\mathcal{B}_{\mathbf{y}}\right]+w_h^j\int_{\mathcal{B}}G(\mathbf{x},\mathbf{y})\Phi_j^{\mathcal{B}}(\mathbf{y})\,\mathrm{d}\mathcal{B}_{\mathbf{y}}\right\}=0. \tag{52}$$

Remark 1. *We point out that the approximation spaces V_h^k and W_h^k are chosen with the same polynomial degree k to guarantee a more accurate approximation of the BI-NRBC. As we will see, in Section 4 Example 1, this choice allows to obtain the expected order of convergence $k+1$ of the global scheme, under the assumption that all the integrals involved in the computation of the matrix entries of the final linear system are computed with a sufficient accuracy.*

We remark however that it is possible in principle to couple discretization spaces with different orders of accuracy. Indeed, as we will show in Section 4 Example 1, we have considered the particular choice of the spaces V_h^2 and W_h^1, that allows to retrieve an accurate solution, even if the optimal order has not been reached. It is worth noting however that, in a more general setting,

different values of k would require a non conforming coupling between the problem defined in the interior computational domain and that defined in the exterior region. A possible remedy could be to enforce weakly the BI-NRBC by a mortar type technique (see for example [14]). Such an approach offers the further advantage of coupling different types of approximation spaces and of using fast techniques for the discretization of the BI-NRBC (see for example the very recent papers [16, 18, 19]). This will be the subject of a future investigation.

To detail the computation of the integrals in (52), due to the arbitrariness of the choice of the contour $\mathcal{B}$, we assume that it is defined either by a global or by a piece-wise (local) parametric representation. In what follows, for simplicity, we consider the case of a global parametrization given by $\mathbf{x} := \boldsymbol{\xi}(\sigma)$ and $\mathbf{y} := \boldsymbol{\xi}(\vartheta)$ with $\sigma, \vartheta \in [0, 2\pi]$. Thus, the integration over $\mathcal{B}$ is reduced to an equivalent integration over the parametric interval $[0, 2\pi]$ and Equation (52) can be rewritten as

$$\sum_{j \in \mathcal{S}^{\mathcal{B}}} \left\{ u_h^j \left[\frac{1}{2}\phi_j^{\mathcal{B}}(\sigma) + \int_0^{2\pi} \frac{\partial G}{\partial \mathbf{n}_\vartheta}(\sigma, \vartheta)\phi_j^{\mathcal{B}}(\vartheta)|\boldsymbol{\xi}'(\vartheta)|\,\mathrm{d}\vartheta \right] + w_h^j \int_0^{2\pi} G(\sigma, \vartheta)\phi_j^{\mathcal{B}}(\vartheta)|\boldsymbol{\xi}'(\vartheta)|\,\mathrm{d}\vartheta \right\} = 0 \quad (53)$$

where $\phi_j^{\mathcal{B}}(\vartheta) := \Phi_j^{\mathcal{B}}(\boldsymbol{\xi}(\vartheta)) = \Phi_j^{\mathcal{B}}(\mathbf{y})$, $\phi_j^{\mathcal{B}}(\sigma) := \Phi_j^{\mathcal{B}}(\boldsymbol{\xi}(\sigma)) = \Phi_j^{\mathcal{B}}(\mathbf{x})$ and, by abuse of notation, we have denoted by $K(\sigma, \vartheta) := K(\boldsymbol{\xi}(\sigma), \boldsymbol{\xi}(\vartheta))$, $K = G, \frac{\partial G}{\partial \mathbf{n}_\vartheta}$.

By enforcing Equation (53) at $N_{\mathcal{B}} := |\mathcal{S}^{\mathcal{B}}|$ (cardinality of $\mathcal{S}^{\mathcal{B}}$) collocation points $\sigma_i \in [0, 2\pi]$ such that $\mathbf{x}_i^c = \boldsymbol{\xi}(\sigma_i) \in \mathcal{B}$, we obtain:

$$\sum_{j \in \mathcal{S}^{\mathcal{B}}} u_h^j \left[\frac{1}{2}\phi_j^{\mathcal{B}}(\sigma_i) + \int_0^{2\pi} \frac{\partial G}{\partial \mathbf{n}_\mathbf{y}}(\sigma_i, \vartheta)\phi_j^{\mathcal{B}}(\vartheta)|\boldsymbol{\xi}'(\vartheta)|\,\mathrm{d}\vartheta \right] + \sum_{j \in \mathcal{S}^{\mathcal{B}}} w_h^j \int_0^{2\pi} G(\sigma_i, \vartheta)\phi_j^{\mathcal{B}}(\vartheta)|\boldsymbol{\xi}'(\vartheta)|\,\mathrm{d}\vartheta = 0, \quad (54)$$

that, by using the notation introduced in the previous section, can be rewritten in matrix form as follows

$$\left(\frac{1}{2}\mathbb{N} + \mathbb{K}\right)\mathbf{u}^{\mathcal{B}} + \mathbb{V}\mathbf{w} = \mathbf{0}, \quad (55)$$

where the generic elements of the matrices $\mathbb{V}$, $\mathbb{K}$ and $\mathbb{N}$ are

$$\mathbb{V}_{ij} := \int_0^{2\pi} G(\sigma_i, \vartheta)\phi_j^{\mathcal{B}}(\vartheta)|\boldsymbol{\xi}'(\vartheta)|\,\mathrm{d}\vartheta \qquad i, j = 1, \ldots, N_{\mathcal{B}} \quad (56)$$

$$\mathbb{K}_{ij} := \int_0^{2\pi} \frac{\partial G}{\partial \mathbf{n}_\mathbf{y}}(\sigma_i, \vartheta)\phi_j^{\mathcal{B}}(\vartheta)|\boldsymbol{\xi}'(\vartheta)|\,\mathrm{d}\vartheta \qquad i, j = 1, \ldots, N_{\mathcal{B}} \quad (57)$$

$$\mathbb{N}_{ij} := \phi_j^{\mathcal{B}}(\sigma_i) \qquad i, j = 1, \ldots, N_{\mathcal{B}}. \quad (58)$$

By combining (48) with (55) we obtain the final linear system

$$\begin{bmatrix} -\mathbb{A}^{\mathcal{B}\mathcal{B}} + \kappa^2\mathbb{M}^{\mathcal{B}\mathcal{B}} & -\mathbb{A}^{\mathcal{B}I} + \kappa^2\mathbb{M}^{\mathcal{B}I} & \mathbb{Q}^{\mathcal{B}\mathcal{B}} \\ -\mathbb{A}^{I\mathcal{B}} + \kappa^2\mathbb{M}^{I\mathcal{B}} & -\mathbb{A}^{II} + \kappa^2\mathbb{M}^{II} & \mathbb{O}^{I\mathcal{B}} \\ \frac{1}{2}\mathbb{N} + \mathbb{K} & \mathbb{O}^{\mathcal{B}I} & \mathbb{V} \end{bmatrix} \begin{bmatrix} \mathbf{u}^{\mathcal{B}} \\ \mathbf{u}^I \\ \mathbf{w} \end{bmatrix} = \begin{bmatrix} (\mathbb{A}^{\mathcal{B}\Gamma} - \kappa^2\mathbb{M}^{\mathcal{B}\Gamma})\mathbf{g} \\ (\mathbb{A}^{I\Gamma} - \kappa^2\mathbb{M}^{I\Gamma})\mathbf{g} \\ \mathbf{0}^{\mathcal{B}} \end{bmatrix} \quad (59)$$

which represents the matrix form of (13).

Remark 2. *We remark that, in the forthcoming numerical tests, the collocation points $\mathbf{x}_i^c = \boldsymbol{\xi}(\sigma_i) \in \mathcal{B}$ will be chosen either nodal or shifted. In the first case they coincide with the mesh nodes detected on $\mathcal{B}$ by the partitioning $\mathcal{T}_h$ of the computational domain Ω while, in the second case, they*

will be obtained by a proper shift of the mesh nodes by the quantity $\delta\Delta\vartheta$, $\Delta\vartheta$ being the mesh size of the parameterization interval and $\delta \in (0,1)$ properly chosen. This alternative choice will depend on the shape of the artificial boundary $\mathcal{B}$ (smooth or with corners) and will be specified in each of the forthcoming numerical examples.

Remark 3. *To compute the integrals in (56)-(57), we generally follow the numerical strategy proposed in [22]. In particular, we apply a standard ν-point Gauss-Legendre quadrature rule when the kernel functions are smooth. We remark however that the kernel G involved in (56) (see formula (4)) has a log-singularity for $r = \|\boldsymbol{\xi}(\sigma_i) - \boldsymbol{\xi}(\vartheta)\| \to 0$. For this reason an accurate computation, by a standard Gaussian rule, of those integrals for which r is small would require a large number ν of quadrature nodes, thus affecting the efficiency of the method. Moreover, since the log-singularity cannot be factored out, it cannot be taken as weight function of the corresponding integrals we have to compute. This means that the use of associated (weighted) Gaussian rules is not an effective approach as well. Therefore, to compute efficiently these integrals, we will use the smoothing strategy proposed in [26] and already applied in several similar contexts (see [22]). This approach consists in the preliminary introduction of a very simple polynomial smoothing change of variable and in the computation of the transformed integrals by a standard ν-point Gauss-Legendre quadrature rule. In particular, denoting by $[\sigma_*, \sigma^*]$ the subinterval of the support in which the basis function $\phi_j^{\mathcal{B}}$ is smooth, if $\sigma_i \in [\sigma_*, \sigma^*]$, we split the integral over $[\sigma_*, \sigma^*]$ as follows:*

$$\int_{\sigma_*}^{\sigma^*} G(\sigma_i,\vartheta)\phi_j^{\mathcal{B}}(\vartheta)|\boldsymbol{\xi}'(\vartheta)|\,\mathrm{d}\vartheta = \int_{\sigma_*}^{\sigma_i} G(\sigma_i,\vartheta)\phi_j^{\mathcal{B}}(\vartheta)|\boldsymbol{\xi}'(\vartheta)|\,\mathrm{d}\vartheta + \int_{\sigma_i}^{\sigma^*} G(\sigma_i,\vartheta)\phi_j^{\mathcal{B}}(\vartheta)|\boldsymbol{\xi}'(\vartheta)|\,\mathrm{d}\vartheta, \qquad (60)$$

and we introduce the change of variable $\vartheta = \sigma_i \pm \eta^q$ with an odd $q > 1$. The sign of the change of variable in the above integrals is minus (plus) when σ_i is the upper (lower) integration endpoint. We remark that, in the nodal collocation case, σ_i coincides with one of the two endpoints (consequently one of the two integrals in (60) is null), while in the shifted collocation case it will be an interior point. The choice of the smoothing parameter q and of the number of quadrature nodes ν depends on the accuracy required for the computation of the matrix entries and influences the accuracy of the global scheme. Therefore, such a choice will depend on the order k of the scheme and will be specified in the numerical tests of Section 4.

4. Numerical examples

In this section we present some numerical examples to validate the accuracy and efficiency of the proposed approach. To this aim, some preliminary features need to be addressed.

For the generation of the partitioning $\mathcal{T}_h$ of the computational domain Ω, we have used the GMSH software (see [23]). In particular, we have built unstructured conforming meshes consisting of quadrilaterals, by employing the Mesh.ElementOrder option within the GMSH code. To simplify the creation of the meshes, in all the examples, we have generated the decomposition of the computational domain in such a way that the points inherited both on Γ and $\mathcal{B}$ are equally spaced. We remark however that this choice does not represent a limit in the applicability of the proposed method.

Out of an extensive numerical testing, for the chosen wave numbers κ, we have considered the stabilization term in (33) for the computation of the stiffness matrix, while that for the evaluation of the mass matrix in (34) has been neglected. This latter, indeed, revealed to be not necessary to achieve a stable solution, in accordance with what observed in [1] and [9].

In the description of the method we have assumed that both the interior and the artificial boundaries of the computational domain Ω are polygonal. As we will see in Example 1, this choice guarantees the optimal convergence rate of the scheme. However, we have also tested our approach in the case of non polygonal boundaries and for more challenging problems; even if in these cases we have retrieved only a sub-optimal rate of convergence, we have obtain very satisfactory numerical results.

To test our numerical approach, the order k of the approximation spaces has been fixed equal to 1 and 2 and it is the same for both V_h^k and W_h^k. In Example 1, we have also considered the approximation spaces V_h^2 and W_h^1 of decoupled orders, which allowed to retrieve an accurate solution despite the loss of the optimal order of convergence. In all the numerical examples, for the computation of integrals that define the entries $\mathbb{V}_{ij}$ in (56), we have applied the q-smoothing strategy and ν-point Gauss-Legendre quadrature rule described in Remark 3, with the following choices:

i) $\nu = 8$ and $q = 3$, if $k = 1$;

ii) $\nu = 8$ for $i \neq j$, $\nu = 16$ for $i = j$ and $q = 5$, if $k = 2$.

This choice of the parameters has guaranteed the computation of the mentioned integrals with a full precision accuracy (16-digit double precision arithmetic) for $k = 1$ and a single precision (8-digit double precision arithmetic) for $k = 2$. This latter is the maximum reached precision with the chosen quadrature number of nodes ν. A higher value of ν could be considered, but it would increase the overall computational cost and imply a not worthy performance of the method.

All the numerical computations have been performed on a PC with Intel® Core™ i7-7700 (3.60 GHz) by means of standard (i.e. sequential) Matlab® codes.

Example 1. We consider here Problem (1), where Ω_e is the outer region of the square $\Omega_i = (-1, 1)^2$. On the boundary Γ we prescribe the Dirichlet condition

$$g(\mathbf{x}) = H_0^{(1)}(\kappa|\mathbf{x} - \mathbf{x}_0|) \qquad \text{with} \quad \mathbf{x}_0 = (-0.25, 0)^\top, \quad \mathbf{x} \in \Gamma \tag{61}$$

where, we recall, $H_0^{(1)}$ denotes the 0-th order Hankel function of the first kind. In this case, the exact solution $u_e(\mathbf{x})$ is known and it is the field produced by the point source at $\mathbf{x}_0$. Its expression is given by (61) for every $\mathbf{x} \in \mathbf{R}^2$.

The aim of this example is to test the accuracy order of the proposed method. To this end, as artificial boundary $\mathcal{B}$ we choose the contour of the square $[-2, 2]^2$ so that the finite computational domain Ω is the frame bounded internally by Γ and externally by $\mathcal{B}$. We remark that this choice avoids the issue of the approximation of the geometry and allows the use of standard (non curvilinear) VEM and BEM methods, without affecting the convergence order of the global scheme.

We start by considering the coarse mesh associated to the level of refinement zero (lev. 0) and all the successive refinements are obtained by halving each side of its elements. In Figure 2, the meshes corresponding to level 0 (left plot) and level 3 (right plot) are represented. In Table 1, we report the total number of degrees of freedom of the VEM space, associated to each decomposition of the computational domain, for the approximation orders $k = 1$ (linear) and $k = 2$ (quadratic). We remark that, due to the technical computer specifications, the maximum level of refinement we have been able to consider is lev. 8 for $k = 1$, whose number of degrees of freedom coincides with that of lev. 7 for $k = 2$.

For what concerns the approximation of the BI-NRBC, due to the presence of corners in the artificial boundary, we choose the *shifted* collocation approach (see Remark 2). This consists in shifting the mesh nodes, defined in the parametrization interval, towards the right by $\delta\Delta\vartheta$, with $\delta = 1/3$. As noticed in [22], any value of δ not too close to one of the values $0, 1/2, 1$ would be an equally good choice.

	lev. 0	lev. 1	lev. 2	lev. 3	lev. 4	lev. 5	lev. 6	lev. 7	lev. 8
$k = 1$	36	120	432	1,632	6,336	24,960	99,072	394,752	1,575,940
$k = 2$	120	432	1,632	6,336	24,960	99,072	394,752	1,575,940	-

Table 1: Example 1. Total number of d.o.f for different levels of refinement and for approximation orders $k = 1, 2$.

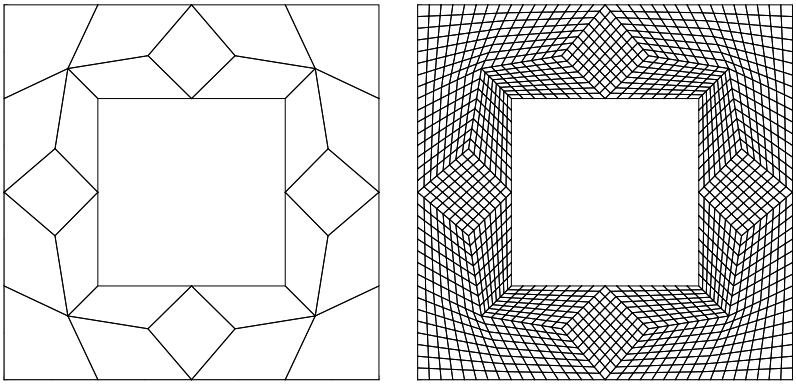

Figure 2: Example 1. Meshes of Ω for lev. 0 (left plot) and lev. 3 (right plot).

In the sequel, we report the numerical results corresponding to the two choices of the wave number $\kappa = 1$ and $\kappa = 10$. In Figures 3 and 4, we show the real and imaginary parts of the numerical solution for $\kappa = 1$ and $\kappa = 10$ respectively, obtained by the quadratic approximation associated to the minimum refinement level for which the graphical behaviour is accurate and not wavy; this latter is lev. 3 for Figure 3 and lev. 5 for Figure 4. We remark that the solution obtained by the linear approximation is graphically accurate choosing lev. 6 for $\kappa = 1$ and lev. 8 for $\kappa = 10$. For brevity we omit to report the corresponding plots.

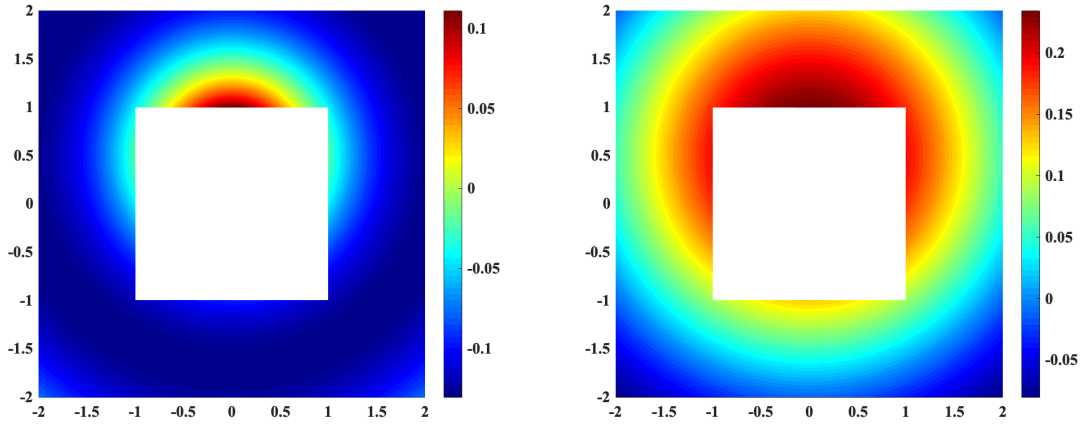

Figure 3: Example 1. Real (left plot) and imaginary (right plot) part of the numerical solution for $\kappa = 1$, refinement lev. 3 and $k = 2$.

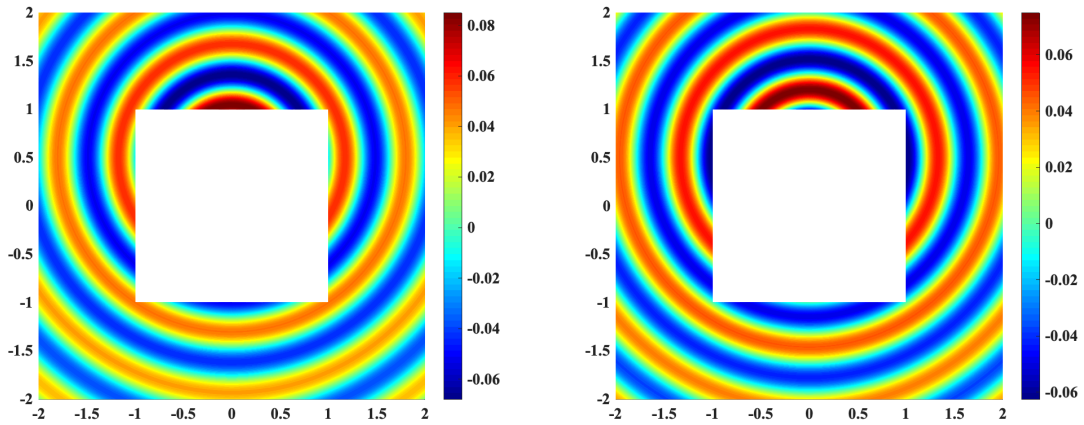

Figure 4: Example 1. Real (left plot) and imaginary (right plot) part of the numerical solution for $\kappa = 10$, refinement lev. 5 and $k = 2$.

In Table 2, we report the L^2-norm errors $\varepsilon^k_{\text{lev}}$ (see [11]) and the corresponding Estimated Order of Convergence (EOC), defined by the formulas

$$\varepsilon^k_{\text{lev}} := \sqrt{\frac{\sum\limits_{E\in\mathcal{T}_h} \left\| u - \Pi^{0,E}_k u_h \right\|^2_{L^2(E)}}{\sum\limits_{E\in\mathcal{T}_h} \|u\|^2_{L^2(E)}}}, \tag{62}$$

$$\text{EOC} := \log_2\left(\frac{\varepsilon^k_{\text{lev}+1}}{\varepsilon^k_{\text{lev}}}\right), \tag{63}$$

where the superscript $k = 1, 2$ refers to the linear or quadratic order approximation of u, the subscript $\text{lev} = 0, \ldots, 8$ ($k = 1$) and $\text{lev} = 0, \ldots, 7$ ($k = 2$) refers to the refinement level and, we recall, $\Pi^{0,E}_k$ is the local L^2-projector defined in (19).
As we can see, for both wave numbers $\kappa = 1$ and $\kappa = 10$, the convergence rate of the scheme is optimal (quadratic) when the linear VEM ($k = 1$) is considered. Instead, in the case of the quadratic VEM ($k = 2$) and starting from lev. 5, the optimal (cubic) convergence rate deteriorates when the wave number $\kappa = 1$ is considered. We recall that this phenomenon is due to the precision reached by the numerical quadrature employed for the computation of the BEM matrix entries, as previously remarked. It is worth noting that for $\kappa = 10$ the optimal convergence rate is indeed preserved since, in this case, the accuracy of the approximation is lower than the single precision.

Finally we note that, as expected, for a fixed refinement level, the accuracy of the solution deteriorates for $\kappa = 10$ with respect to $\kappa = 1$ since the density of points per wavelength $\lambda = {}^{2\pi}/_{\kappa}$ decreases when κ increases.

		$\kappa = 1$				$\kappa = 10$			
lev	h	$\varepsilon^1_{\text{lev}}$	EOC	$\varepsilon^2_{\text{lev}}$	EOC	$\varepsilon^1_{\text{lev}}$	EOC	$\varepsilon^2_{\text{lev}}$	EOC
0	$1.86e+00$	$7.02e-02$		$1.02e-02$		$1.04e+00$		$3.00e+00$	
			1.8		2.9		0.0		2.6
1	$9.45e-01$	$1.98e-02$		$1.34e-03$		$1.02e+00$		$5.06e-01$	
			1.9		3.2		0.8		2.3
2	$4.77e-01$	$5.18e-03$		$1.48e-04$		$5.90e-01$		$1.02e-01$	
			2.0		3.0		0.8		3.2
3	$2.40e-01$	$1.31e-03$		$1.81e-05$		$3.43e-01$		$1.15e-02$	
			2.0		2.9		1.8		3.2
4	$1.20e-01$	$3.28e-04$		$2.38e-06$		$9.53e-02$		$1.23e-03$	
			2.0		2.7		2.1		3.4
5	$6.02e-02$	$8.20e-05$		$3.58e-07$		$2.25e-02$		$1.14e-04$	
			2.0		2.4		2.0		3.4
6	$3.01e-02$	$2.05e-05$		$6.67e-08$		$5.54e-03$		$1.06e-05$	
			2.0		2.2		2.0		3.3
7	$1.50e-02$	$5.12e-06$		$1.50e-08$		$1.38e-03$		$1.08e-06$	
			2.0		×		2.0		×
8	$7.52e-03$	$1.28e-06$		×		$3.45e-04$		×	

Table 2: Example 1. Relative errors in L^2-norm and EOC for wave numbers $\kappa = 1, 10$ and approximation orders $k = 1, 2$.

For completeness, in Figure 5, we show the sparsity patterns of the matrices associated to the final linear system (59) which give an idea of the memory requirement of the BEM with respect to the VEM. As we can see the matrix system exhibits a block structure in which the BEM matrices are fully populated and, in general, non symmetric. This is in contrast to the VEM blocks, that are sparse and symmetric. As expected, as the problem size (d.o.f.) grows, the BEM blocks become smaller and negligible, compared to the VEM ones, and the global system matrix can be considered sparse. Consequently, we expect that the global complexity scales linearly as that of the VEM. This is confirmed by the behaviour of the total memory storage with respect to the increasing number of d.o.f., which is reported in Figure 6. We observe that the complexity is optimal for both approximation orders $k = 1, 2$.

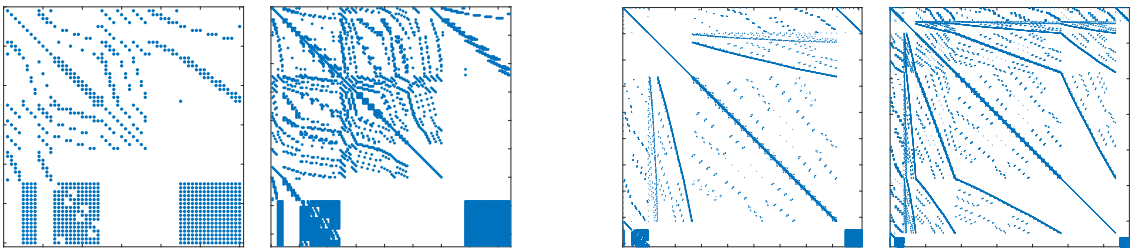

Figure 5: Sparsity patterns of the global system matrix for lev. 0 (left plots, $k = 1$ on the left and $k = 2$ on the right) and lev. 3 (right plots, $k = 1$ on the left and $k = 2$ on the right).

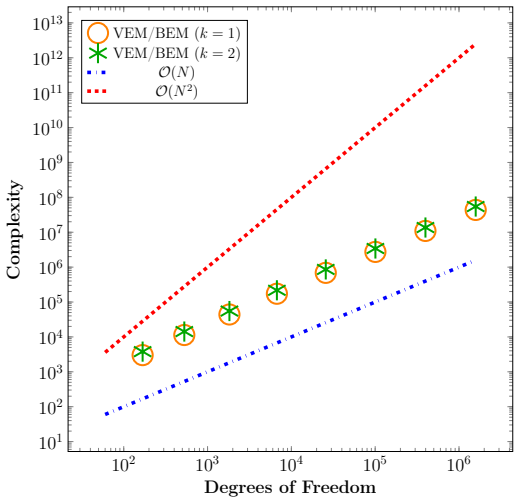

Figure 6: Memory storage with respect to d.o.f.

As previously remarked, the choice of the same approximation order of the spaces V_h^k and W_h^k is necessary to obtain the optimal convergence order. As a further investigation, we have considered the spaces V_h^2 and W_h^1. This is a manageable setting from the implementation point of view, since it is possible to enforce the conforming coupling of the VEM with the BI-NRBC by discretizing this latter using piecewise linear polynomials defined on the finer mesh inherited on $\mathcal{B}$ from the degrees of freedom of the VEM. In Table 3, we report the corresponding numerical L^2-norm relative errors, denoted by $\varepsilon_{\text{lev}}^{2,1}$, where we observe that the convergence order seems to be only linear.

		$\kappa = 1$		$\kappa = 10$	
lev	h	$\varepsilon_{\text{lev}}^{2,1}$	EOC	$\varepsilon_{\text{lev}}^{2,1}$	EOC
0	$1.86e+00$	$2.32e-02$		$1.04e+00$	
			1.6		0.8
1	$9.45e-01$	$7.76e-03$		$5.87e-01$	
			1.3		0.2
2	$4.77e-01$	$3.16e-03$		$5.23e-01$	
			1.2		2.4
3	$2.40e-01$	$1.42e-03$		$9.63e-02$	
			1.1		2.1
4	$1.20e-01$	$6.72e-04$		$2.21e-02$	
			1.0		1.8
5	$6.02e-02$	$3.27e-04$		$6.25e-03$	
			1.0		1.5
6	$3.01e-02$	$1.61e-04$		$2.24e-03$	
			1.0		1.2
7	$1.50e-02$	$8.01e-05$		$9.81e-04$	

Table 3: Example 1. Relative errors in L^2-norm and EOC for wave numbers $\kappa = 1, 10$ and decoupled approximation orders.

Example 2. We apply our numerical scheme to simulate the phenomenon of the wave propagation in its spinning mode around an obstacle Ω_i, whose boundary Γ is the circumference of radius $R_0 = 1$ centred at the origin of the Cartesian axes. This benchmark example is taken from [20]. The solution of this problem is known and it is given in polar coordinates (r, θ) by:

$$u_{\text{spin}}(r, \theta) = H_m^{(2)}(\kappa r) e^{-\imath m \theta}, \tag{64}$$

where $H_m^{(2)}$ represents the Hankel function of the second kind of m-th order. The parameter m defines the number of waves in the polar direction and is fixed here $m = 30$. Moreover, choosing the wave number $\kappa = 40$, we deal with a problem in the high-frequency regime since $2\kappa R_0 = 80$. For this choice of the parameters, it is known that the sound wave propagates with a slow decay rate of order $1/\sqrt{r}$, as prescribed by the Sommerfield radiation condition.
We consider Problem (1) with Dirichlet datum $g = u_{\text{spin}}$ on Γ. We reduce the infinite domain Ω_e to an annulus Ω bounded internally by Γ and externally by the circular artificial boundary $\mathcal{B}$ of radius $R_1 = 2$ centered at the origin. We remark that, since the computational domain has a non-polygonal shape, the polygonal mesh $\mathcal{T}_h$ introduces an approximation Ω_h of Ω, by means of an inscribed polygon.
We consider two meshes: the first consisting of $N_{\text{E}} = 81,920$ quadrilaterals and mesh size $h = 3.50e-02$; the second one is obtained by a refinement of the previous one and consists of $N_{\text{E}} = 327,680$ quadrilaterals with $h = 1.75e-02$.
The virtual element space of order $k = 2$ is associated to the coarser mesh, while that of order $k = 1$ to the finer one. The boundary points, inherited on $\mathcal{B}$ from these tessellations, are uniformly spaced in both cases and their number is $N_{\mathcal{B}} = 2,048$. Since in this case the artificial boundary is smooth, for the approximation of the BI-NRBC we have applied the nodal collocation method, using the mesh points as collocation nodes. The two discretizations give rise to a linear system of order $329,216$. With such a choice, the relative errors (62) are about $8.79e-02$ for $k = 1$ and $2.22e-03$ for $k = 2$.
In Figure (7) we plot the real (on the left) and imaginary (on the right) part of the solution obtained with $k = 2$, showing that the propagating mode is well approximated, without the presence of wavy or undulating effects. A very similar graph has been obtained for $k = 1$.

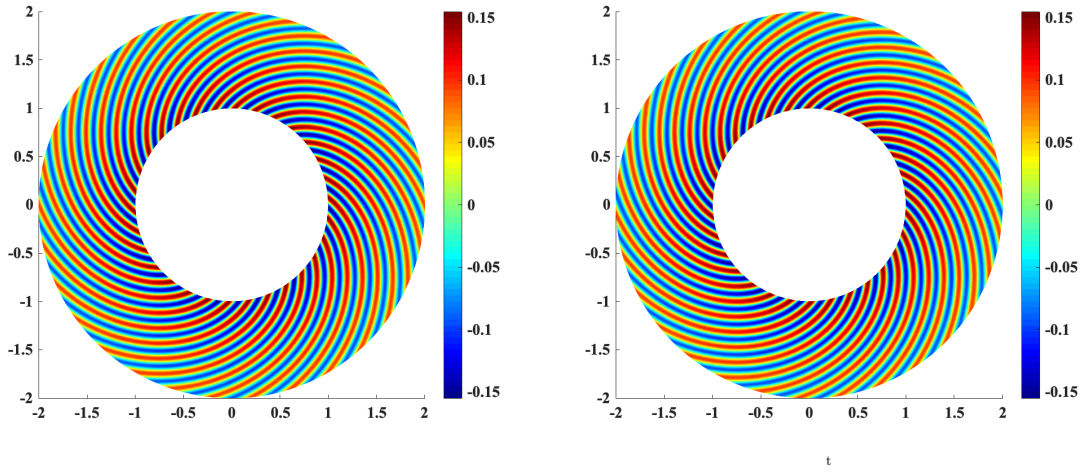

Figure 7: Example 2. Real (left plot) and imaginary (right plot) part of the numerical solution $u_{h,\text{spin}}$ for $\kappa = 40$, $m = 30$ and $k = 2$.

Example 3. In the following examples we consider 3D scattering problems which, under proper geometric and data assumptions, can be reduced to 2D ones. This is the case, for example, of problems defined on the exterior of bounded rigid domains, which are invariant in one of the Cartesian directions. These problems occur in several applications such as acoustics, electromagnetics, optics, elasticity and, generally, involve large values of κ and multiple scatterers.
In particular, we focus here on the scattering of incident plane waves with unit amplitude

$$u_{\text{inc}}(\mathbf{x}) = e^{\imath\kappa x_1}$$

by N_{cyl} infinitely long and equal cylindrical scatterers. In a fixed 3D Cartesian coordinates system $\mathbf{x} = (x_1, x_2, x_3)^\top$, each obstacle is supposed to be invariant with respect to x_3, and to have circular

section with radius R_p centred at point $\mathbf{O}_p$, with $p = 1, \dots, N_{\text{cyl}}$. We set our simulation in the plane $x_3 = 0$, where the scattering obstacle Ω_i is the union of N_{cyl} disks $\Omega_{i,p}$ with boundaries Γ_p, so that the global boundary Γ is the union of the local boundaries Γ_p, $p = 1, \dots, N_{\text{cyl}}$.
The incident wave is scattered by the cylinders in the surrounding medium $\Omega_e = \mathbf{R}^2 \setminus \overline{\cup_{p=1}^{N_{\text{cyl}}} \Omega_{i,p}}$. The scattered field u_{sca} is solution of Problem (1) with Dirichlet datum $g = -u_{\text{inc}}$ on Γ and the total field is retrieved as $u_{\text{tot}}(\mathbf{x}) := u_{\text{inc}}(\mathbf{x}) + u_{\text{sca}}(\mathbf{x})$, $\mathbf{x} = (x_1, x_2, 0)^\top$.

Example 3.1. Scattering of a plane wave by a single cylinder at high-frequency. The first test aims at showing the efficiency of the proposed method to simulate high-frequency problems. We choose the wave number $\kappa = 100$ and we consider a single cylinder whose section Ω_i is the unit disk centred at the origin $\mathbf{O} = (0, 0)^\top$ of the Cartesian axis, so that $2\kappa R = 200$.
In polar coordinates (r, θ), the analytical expression of the scattered wave in Ω_e is given by

$$u_{\text{sca}}(r, \theta) = -\sum_{m=0}^{\infty} (-\imath)^m \epsilon_m \frac{J_m(\kappa R)}{H_m^{(1)}(\kappa R)} H_m^{(1)}(\kappa r) \cos(m\theta), \tag{65}$$

where J_m represents the Bessel function of the first kind of m-th order, while ϵ_m is the Neumann symbol, such that $\epsilon_0 = 1$ and $\epsilon_m = 2$ for $m \geq 1$.
The artificial boundary $\mathcal{B}$ is chosen as the contour of the square centred at the origin with edge 4. We consider two meshes: the first consisting of $N_{\text{E}} = 393,216$ quadrilaterals and mesh size $h = 1.49e-02$; the second one results as a refinement of the previous and consists of $N_{\text{E}} = 1,572,864$ quadrilaterals with $h = 7.45e-03$.
The virtual element space of order $k = 2$ is associated to the coarser mesh, while that of order $k = 1$ to the finer one. Both decompositions induce $N_{\mathcal{B}} = 4,096$ equally spaced points on $\mathcal{B}$ and the corresponding discrete problems have the same number of degrees of freedom $N = 1,575,940$. With such choices the relative L^2-norm errors associated to the reference solution, computed by truncating the series in (65) to $m = 400$, are $2.76e-01$ for $k = 1$ and $7.11e-03$ for $k = 2$.

In Figure 8, we report the absolute value of the computed scattered wave for $k = 1$ (left plot) and $k = 2$ (right plot). As we can see, in accordance with the reported error values, for the same number N of degrees of freedom, the solution obtained by the quadratic VEM/BI-NRBC displays a graphical behaviour more satisfactory than that associated to the linear VEM/BI-NRBC. Indeed this latter shows a spurious and wavy behaviour. The same considerations hold for the absolute value of the total field reported in Figure 9.

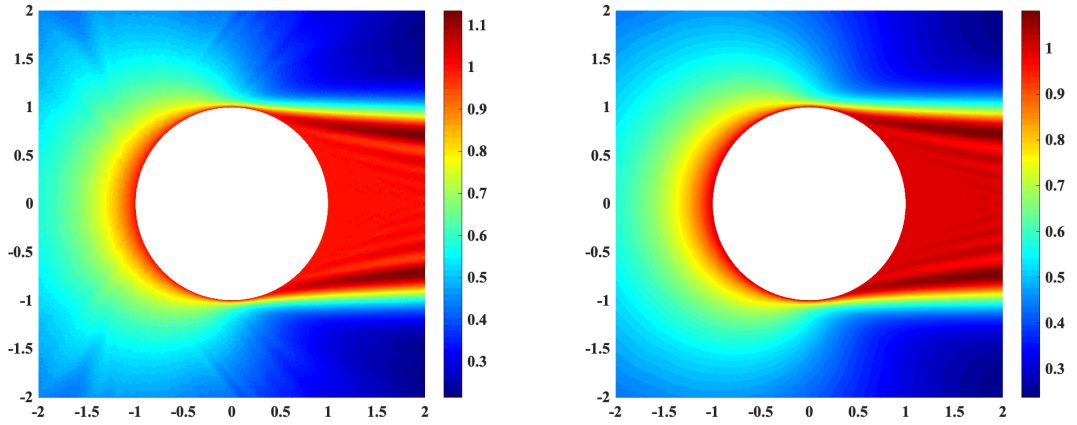

Figure 8: Example 3.1. Absolute value of the scattered wave for $k = 1$ (left plot), $k = 2$ (right plot) and $\kappa = 100$.

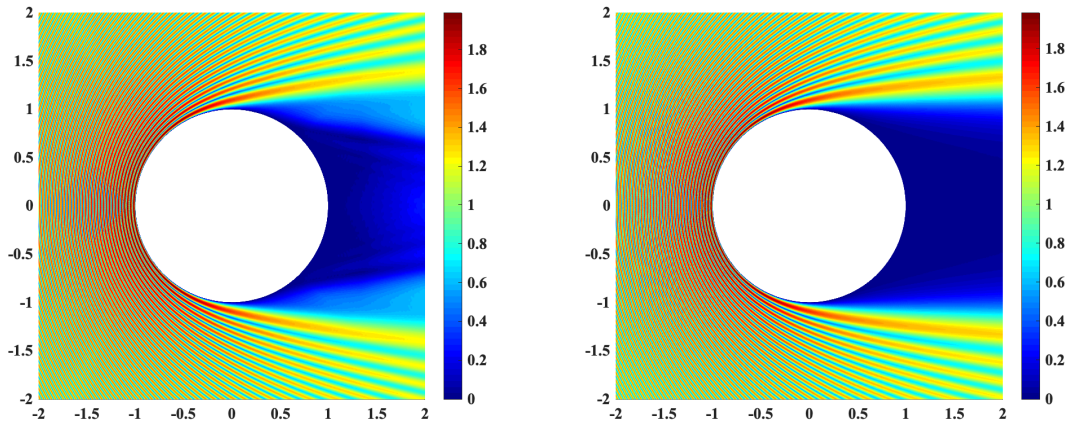

Figure 9: Example 3.1. Absolute value of the total wave for $k = 1$ (left plot), $k = 2$ (right plot) and $\kappa = 100$.

Example 3.2. Scattering of a plane wave by two disjoint cylinders. We consider here the case of two cylindrical obstacles, whose sections $\Omega_{i,1}$ and $\Omega_{i,2}$ have circular boundaries Γ_1 and Γ_2, with radii $R = R_1 = R_2 = 0.5$ and centres $\mathbf{O}_1 = (2, 0)^\top = -\mathbf{O}_2$. We choose the wave number $\kappa = 5$, so that $2\kappa R = 5$ (low-frequency regime).

In order to reduce the infinite domain $\Omega_e = \mathbf{R}^2 \setminus \overline{\Omega_{i,1} \cup \Omega_{i,2}}$ to a computational region Ω of finite extent, we enclose $\Omega_{i,1}$ and $\Omega_{i,2}$ inside the box $[-10, 10]^2$, whose contour defines the artificial boundary $\mathcal{B}$. Thus, Ω is bounded internally by Γ_1 and Γ_2 and externally by $\mathcal{B}$. We consider a decomposition of the computational domain into $N_{\text{E}} = 67,584$ polygons ($h = 3.62e-01$). The total number of equally spaced points on $\mathcal{B}$ is $N_{\mathcal{B}} = 512$. On this tessellation we build a VEM space of order $k = 2$ so that the number of degrees of freedom associated with the final linear system is $N = 272,639$.
Since in the case of multiple scatterers an analytical expression of the scattered wave u_{sca} in Ω_e is not known, we have compared the behaviour of the numerical solution with the reference solution provided in [3] (see Figure 6 top-left plot). In Figure 10, we show the absolute value of the computed scattered (left plot) and total (right plot) waves. By a comparison, we observe that the scattered field perfectly matches with the reference one in [3].

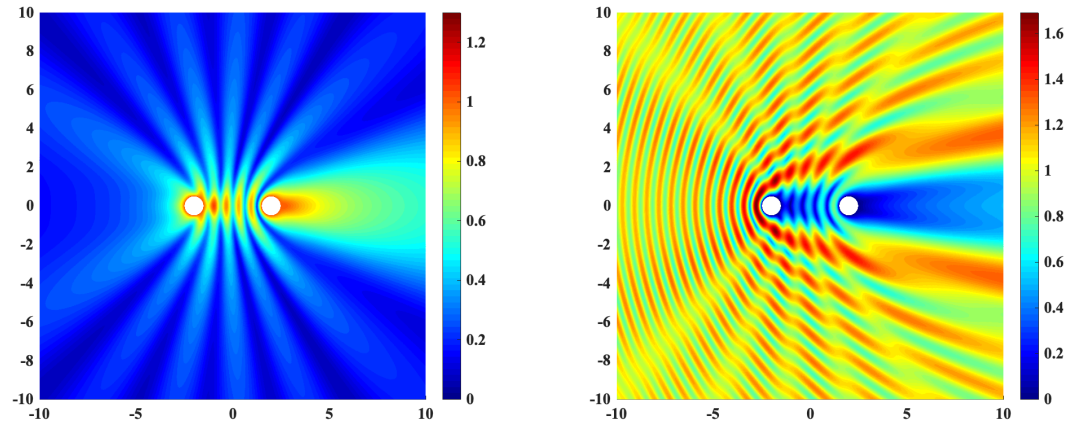

Figure 10: Example 3.2. Absolute value of the scattered (left plot) and total (right plot) wave for $\kappa = 5$ and $k = 2$.

Example 3.3. Scattering of a plane wave by five disjoint cylinders. For the last test, we fix the wave number $\kappa = 5$ and consider five scatterers, whose circular sections $\Omega_{i,p}$ are disks of radius $R = R_p = 0.5$, $p = 1, \cdots, 5$. The corresponding centres are $\mathbf{O}_1 = (0,0)^\top$, $\mathbf{O}_2 = (2,0)^\top = -\mathbf{O}_3$, $\mathbf{O}_4 = (0,2)^\top = -\mathbf{O}_5$. Even if in this case our problem is set in the low-frequency regime, since $2\kappa R = 5$, the reproduction of the scattered field is extremely complex in the region between the obstacles, when these are bumped by the incident wave. Aiming at determining an accurate solution in that region, we surround the scatterers by a proper non convex star-shaped curve, boundary of the star domain ✧ represented in Figure 11. The computational domain $\Omega_{\text{✧}} := \text{✧} \setminus \overline{\cup_{p=1}^{5} \Omega_{i,p}}$ has been decomposed into $N_{\text{E}} = 173,056$ quadrilaterals ($h = 1.43e-01$), and the induced (equally spaced) points on the artificial boundary are $N_{\mathcal{B}} = 1024$. The solution has been obtained by the quadratic VEM/BI-NRBC method and by applying the *shifted* collocation method with $\delta = 1/3$; the total number of degrees of freedom of the final linear system is $N = 512,468$. In Figure 11 we plot the absolute value of the approximated scattered and total field.

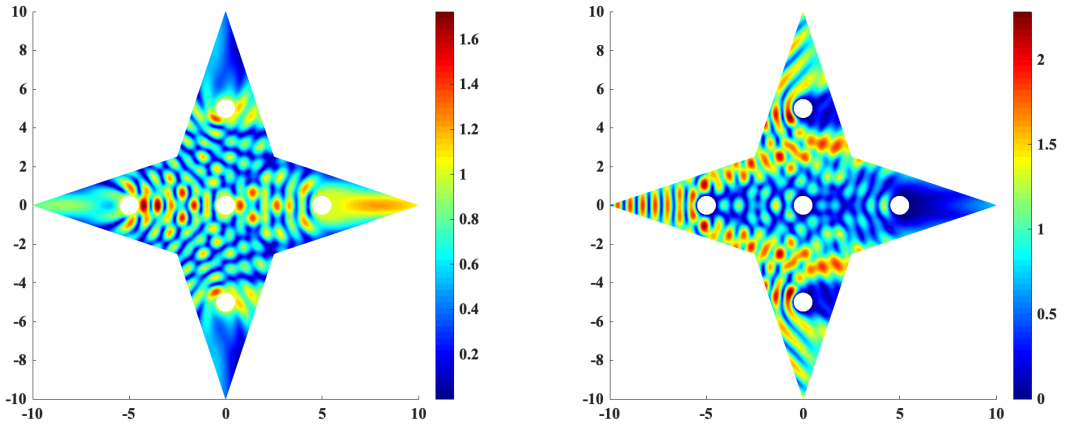

Figure 11: Example 3.3. Absolute value of the scattered (left plot) and total (right plot) wave in $\Omega_{\text{✧}}$ for $\kappa = 5$ and $k = 2$.

To test the applicability of the proposed method in cases of non-convex artificial boundaries with re-entrant corners like the one considered, and hence the reliability of the corresponding numerical results, we compare the above solution with that retrieved in the larger (previously tested) domain $\Omega_{\square}$ obtained by enclosing the obstacles in the box $[-10, 10]^2$.

In Figure 12, we show the absolute value of the computed scattered (left plot) and total (right plot) waves in $\Omega_{\square}$. As we can see, the solutions represented in Figure 11 for $\Omega_{\text{✧}}$ perfectly match with the restriction to $\Omega_{\text{✧}}$of those represented in Figure 12 for $\Omega_{\square}$. It is worth noting that the choice of the larger domain $\Omega_{\square}$ implies a higher computational cost and RAM resource since its decomposition required a number $N_{\text{E}} = 450,560$ of quadrilaterals ($h = 3.46e-01$) and $N_{\mathcal{B}} = 512$ points on $\mathcal{B}$ to achieve a reliable solution. With such a choice, the total number of degrees of freedom for the problem defined in $\Omega_{\square}$ is $N = 1,353,468$.

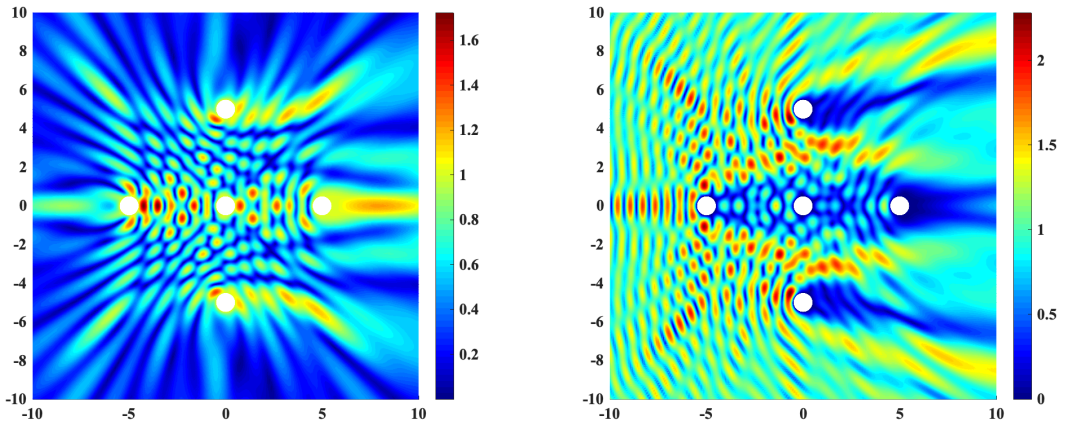

Figure 12: Example 3.3. Absolute value of the scattered (left plot) and total (right plot) wave in $\Omega_{\square}$ for $\kappa = 5$ and $k = 2$.

5. Conclusions and perspectives

We have proposed a new approach for solving 2D Helmholtz problems defined in unbounded regions, external to bounded obstacles. The novelty of this paper consists in using a Virtual Element Method as domain method (instead of standard ones such as Finite Elements or Finite Differences) to determine the solution in a computational domain limited by an artificial boundary. The main benefits of the VEMs, we have exploited here, are the use of generic, non triangular, meshes associated to discrete spaces of order k, not necessarily of linear type. In particular, the VEM allows to use approximation orders $k > 1$ by knowing the explicit expression of the virtual element basis functions only on the mesh elements boundary. This feature facilitates the practical implementation of the corresponding method for high values of k. To guarantee a well posed problem in the finite computational domain and an optimal convergence order, we have combined the VEM with a collocation BEM of the same order k; the latter has been applied for the discretization of an integral non reflecting condition imposed on the artificial boundary.

We have applied our approach to multiple scattering problems from the low to the high frequency regime, treated in literature and/or arising from real life application problems. By an extensive numerical testing, we have shown the expected optimal order of convergence of the global scheme. Moreover, by a comparison with the papers from which our tests have been drawn on, the scheme revealed to be accurate and competitive. We remark that, at the current implementation stage, we have limited the choice of $k = 1, 2$ since a higher approximation order for the discretization of the BI-NRBC would require proper numerical strategies for the accurate computation of the BEM matrix entries. This issue, as already observed in other contexts, is crucial to maintain the overall accuracy but is out of the aim of the present pioneering paper. Furthermore, a possible extension of this work, which has been presented in the homogeneous case, consists in considering inhomogeneous media and in applying the VEM in the subregion which contains different physical properties. We recall that, to obtain the solution of an exterior homogeneous problem in a wide region, the use of the VEM has a computational cost significantly lower than that of a pure BEM approach. To retrieve the problem solution, the latter would require the evaluations of a very large number of boundary integrals. When inhomogeneities are considered, the proposed VEM coupled with BI-NRBC offers not only the advantage of reducing the computational cost, but also of treating a problem for which a pure BEM could not be applied, the associated fundamental solution being not known in this case. Since these aspects are worth to be studied, they will be the subject of future investigations.

Acknowledgments

This work was performed as part of the GNCS-IDAM 2020 research program *"Metodologie innovative per problemi di propagazione di onde in domini illimitati: aspetti teorici e computazionali"*. The second and the third author were partially supported by MIUR grant *"Dipartimenti di Eccellenza 2018-2022"*, CUP E11G18000350001.

References

[1] B. Ahmed, A. Alsaedi, F. Brezzi, L. D. Marini and A. Russo, Equivalent projectors for virtual element methods, *Computers & Mathematics with Applications*, **66** (2013), pp. 376–391.

[2] A. Aimi, L. Desiderio, M. Diligenti and C. Guardasoni, A numerical study of energetic BEM-FEM applied to wave propagation in 2D multidomains, *Publications de l'Institut Mathématique*, **96**, 110 (2014), pp. 5–22.

[3] H. Alzubaidi, X. Antoine and C. Chniti, Formulation and accuracy of On-Surface Radiation Conditions for acoustic multiple scattering problems, *Applied Mathematics and Computation*, **277**, (2016), pp. 82–100.

[4] P.F. Antonietti, L. Beirão da Vega, D. Mora and M.A. Verani, A stream virtual element formulation of the Stokes problem on polygonal meshes, *SIAM Journal of Numerical Analysis*, **52**,1 (2014), pp. 386–404.

[5] E. Artioli, L. Beirão da Vega, C. Lovadina and E. Sacco, Arbitrary order 2D virtual elements for polygonal meshes: Part II, inelastic problem, *Computational Mechanics*, **60**,4 (2017), pp. 643–657.

[6] L. Banjai, C. Lubich and F-J. Sayas, Stable numerical coupling of exterior and interior problems for the wave equation, *Numerische Mathematik*, **129**, 4 (2015), pp. 611–646.

[7] L. Beirão da Vega, F. Brezzi, A. Cangiani, G. Manzini, L.D. Marini and A. Russo, Basic principles of virtual element method, *Mathematical Models and Methods in Applied Sciences* **23**,1 (2013), pp. 199–214.

[8] L. Beirão da Vega, F. Brezzi and L.D. Marini, Virtual elements for linear elasticity problems, *SIAM Journal of Numerical Analysis* **51**,2 (2013), pp. 794–812.

[9] L. Beirão da Vega, F. Brezzi, L.D. Marini and A. Russo, The hitchhiker's guide to the virtual element method, *Mathematical Models and Methods in Applied Sciences* **24**,8 (2014), pp. 1541–1573.

[10] L. Beirão da Vega, F. Brezzi, L.D. Marini and A. Russo, Virtual element method for general second order elliptic problems on polygonal meshes, *Mathematical Models and Methods in Applied Sciences* **26**,4 (2016), pp. 729–750.

[11] L. Beirão da Vega, A. Russo and G. Vacca, The Virtual Element Method with curved edges, *ESAIM: Mathematical Modelling and Numerical Analysis*, **53**,2 (2019), pp. 375–404.

[12] M. F. Benedetto, S. Berrone, S. Pieraccini, and S. Scialò, The virtual element method for discrete fracture network simulations, *Computer Methods in Applied Mechanics and Engineering*, **280**,1 (2014), pp. 135–156.

[13] M. F. Benedetto, S. Berrone, A. Borio, S. Pieraccini and S. Scialò, A hybrid mortar virtual element method for discrete fracture network simulations, *Journal of Computational Physics*, **306** (2016), pp. 148–166.

[14] S. Bertoluzza and S. Falletta, FEM Solution of Exterior Elliptic Problems with Weakly Enforced Integral Non Reflecting Boundary Conditions, *Journal of Scientific Computing* , **81**,2 (2019), pp. 1019–1049.

[15] F. Brezzi and L.D. Marini, Virtual element methods for plate bending problems, *Computer Methods in Applied Mechanics and Engineering* **253** (2013), pp. 455–462.

[16] S. Chaillat, L. Desiderio and P. Ciarlet, Theory and implementation of $\mathcal{H}$-matrix based iterative and direct solvers for Helmholtz and elastodynamic oscillatory kernels, *Journal of Computational Physics* **351** (2017), pp. 165–186.

[17] D. Colton and R. Kress, Inverse acoustic and electromagnetic scattering theory, *Applied mathematical sciences*, Springer Berlin Heidelberg, (1997).

[18] L. Desiderio, An $\mathcal{H}$-matrix based direct solver for the boundary element method in 3D elastodynamics, *AIP Conference Proceedings* **1978** (2018), 120005.

[19] L. Desiderio and S. Falletta, Efficient solution of 2D wave propoagation problems by CQ-wavelet BEM: algorithm and applications, *SIAM Journal on Scientific Computing*, **42**,4 (2020), pp. B894–B920.

[20] M. Dinachandra and S. Raju, Plane wave enriched Partition of Unity Isogeometric Analysis (PUIGA) for 2D-Helmholtz problems, *Computer Methods in Applied Mechanics and Engineering*, **335** (2018), pp. 380–402.

[21] S. Falletta and G. Monegato, An exact non reflecting boundary condition for 2D time-dependent wave equation problems, *Wave Motion*, **51**, 1 (2014), pp. 168–192.

[22] S. Falletta, G. Monegato and L. Scuderi, A space-time BIE method for wave equation problems: the (two-dimensional) Neumann case, *IMA Journal of Numerical Analysis*, **34** (1) (2014), pp. 390–434.

[23] C. Geuzaine and J.F. Remacle, Gmsh: a three-dimensional finite element mesh generator with built-in pre- and post processing facilities. *International Journal for Numerical Methods in Engineering* **79** (2009), pp 1309–1331.

[24] D. Givoli, High-order local non-reflecting boundary conditions: a review, *Wave Motion*, **39** (2004), pp. 319–326.

[25] D. Givoli, Numerical Methods for Problems in Infinite Domains. *Elsevier*, (2013).

[26] G. Monegato, L. Scuderi, Numerical integration of functions with boundary singularities, *Journal of Computational and Applied Mathematics*, **112** (1999), pp. 201–214.

[27] I. Perugia, P. Pietra and A. Russo, A plane wave virtual element method for the Helmholtz problem, *ESAIM: Mathematical Modelling and Numerical Analysis* **50**,3 (2016), pp. 783–808.

[28] A. Quarteroni and A. Valli, Numerical Approximation of Partial Differential Equations, *Springer*, Berlin, (1994).

[29] S.A. Sauter and C. Schwab, Boundary Element Methods, *Springer Series in Computational Mathematics*, Vol. **39**, (2010), Springer.

[30] F.J. Sayas, The validity of Johnson-Nédélec's BEM-FEM coupling on polygonal interfaces, *SIAM Journal of Numerical Analysis* **47** (2009), pp. 3451–3463.

[31] M. Schanz and O. Steinbach, Boundary element analysis: mathematical aspects and applications, *Springer Science & Business Media*, Vol. **29**, (2007).

[32] O. Steinbach, A note on the stable one-equation coupling of finite and boundary elements, *SIAM Journal of Numerical Analysis* **49**,4 (2011), pp. 1521–1531.